A high-density, high-channel count, multiplexed μ ECoG array for auditory-cortex recordings

Monty A. Escabí, Heather L. Read, Jonathan Viventi, Dae-Hyeong Kim, Nathan C. Higgins, Douglas A. Storace, Andrew S. K. Liu, Adam M. Gifford, John F. Burke, Matthew Campisi, Yun-Soung Kim, Andrew E. Avrin, Van der Spiegel Jan, Yonggang Huang, Ming Li, Jian Wu, John A. Rogers, Brian Litt and Yale E. Cohen

J Neurophysiol 112:1566-1583, 2014. First published 11 June 2014; doi:10.1152/jn.00179.2013

Journal of Neurophysiology publishes original articles on the function of the nervous system. It is published 12 times a year (monthly) by the American Physiological Society, 9650 Rockville Pike, Bethesda MD 20814-3991. ISSN: 0022-3077, ESSN: 1522-1598. Visit our website at http://www.the-aps.org/.

J Neurophysiol 112: 1566–1583, 2014.
First published June 11, 2014; doi:10.1152/jn.00179.2013.

A high-density, high-channel count, multiplexed μECoG array for auditory-cortex recordings

Monty A. Escabí,[1,2,3]* Heather L. Read,[1,2]* Jonathan Viventi,[4,5] Dae-Hyeong Kim,[6] Nathan C. Higgins,[1] Douglas A. Storace,[1] Andrew S. K. Liu,[7] Adam M. Gifford,[8] John F. Burke,[8] Matthew Campisi,[5] Yun-Soung Kim,[9] Andrew E. Avrin,[10] Jan Van der Spiegel,[10] Yonggang Huang,[12] Ming Li,[13] Jian Wu,[14] John A. Rogers,[9] Brian Litt,[11,15] and Yale E. Cohen[11,16,17]

[1]*Department of Psychology, University of Connecticut, Storrs, Connecticut;* [2]*Department of Biomedical Engineering, University of Connecticut, Storrs, Connecticut;* [3]*Department of Electrical Engineering, University of Connecticut, Storrs, Connecticut;* [4]*Center for Neural Science, New York University, New York, New York;* [5]*Department of Electrical and Computer Engineering, Polytechnic Institute of New York University, Brooklyn, New York;* [6]*Center for Nanoparticle Research of Institute for Basic Science, School of Chemical and Biological Engineering, Seoul National University, Seoul, Republic of Korea;* [7]*Bioengineering Graduate Group, University of Pennsylvania, Philadelphia, Pennsylvania;* [8]*Neuroscience Graduate Group, University of Pennsylvania, Philadelphia, Pennsylvania;* [9]*Department of Materials Science and Engineering, Beckman Institute for Advanced Science and Technology and Frederick Seitz Materials Research Laboratory, University of Illinois at Urbana-Champaign, Urbana, Illinois;* [10]*Department of Electrical and Systems Engineering, University of Pennsylvania, Philadelphia, Pennsylvania;* [11]*Department of Bioengineering, University of Pennsylvania, Philadelphia, Pennsylvania;* [12]*Departments of Mechanical Engineering and Civil and Environmental Engineering, Northwestern University, Evanston, Illinois;* [13]*State Key Laboratory of Structural Analysis for Industrial Equipment, Dalian University of Technology, Dalian, China;* [14]*Department of Engineering Mechanics, Tsinghua University, Beijing, China;* [15]*Department of Neurology, Perelman School of Medicine, University of Pennsylvania, Philadelphia, Pennsylvania;* [16]*Department of Neuroscience, Perelman School of Medicine, University of Pennsylvania, Philadelphia, Pennsylvania; and* [17]*Department of Otorhinolaryngology, Perelman School of Medicine, University of Pennsylvania, Philadelphia, Pennsylvania*

Submitted 11 March 2013; accepted in final form 6 June 2014

Escabí MA, Read HL, Viventi J, Kim DH, Higgins NC, Storace DA, Liu AS, Gifford AM, Burke JF, Campisi M, Kim YS, Avrin AE, Van der Spiegel J, Huang Y, Li M, Wu J, Rogers JA, Litt B, Cohen YE. A high-density, high-channel count, multiplexed μECoG array for auditory-cortex recordings. *J Neurophysiol* 112: 1566–1583, 2014. First published June 11, 2014; doi:10.1152/jn.00179.2013.—Our understanding of the large-scale population dynamics of neural activity is limited, in part, by our inability to record simultaneously from large regions of the cortex. Here, we validated the use of a large-scale active microelectrode array that simultaneously records 196 multiplexed micro-electrocortigraphical (μECoG) signals from the cortical surface at a very high density (1,600 electrodes/cm^2). We compared μECoG measurements in auditory cortex using a custom "active" electrode array to those recorded using a conventional "passive" μECoG array. Both of these array responses were also compared with data recorded via intrinsic optical imaging, which is a standard methodology for recording sound-evoked cortical activity. Custom active μECoG arrays generated more veridical representations of the tonotopic organization of the auditory cortex than current commercially available passive μECoG arrays. Furthermore, the cortical representation could be measured efficiently with the active arrays, requiring as little as 13.5 s of neural data acquisition. Next, we generated spectrotemporal receptive fields from the recorded neural activity on the active μECoG array and identified functional organizational principles comparable to those observed using intrinsic metabolic imaging and single-neuron recordings. This new electrode array technology has the potential for large-scale, temporally precise monitoring and mapping of the cortex, without the use of invasive penetrating electrodes.

electrocorticography; μECoG; auditory cortex; topography; tonotopy

FUTURE LARGE-SCALE BRAIN RECORDINGS in humans and experimental-animal models require methodologies that yield high temporal and spatial precision of recordings across large cortical surface areas in a minimally invasive manner. These applications also could benefit from techniques that allow for rapid simultaneous, continuous data acquisition from large cortical surface areas. However, the resolution and coverage of all current electrode arrays in development for such applications has been limited by the constraint that each electrode is individually connected to external systems. The volume and bulk of these connections typically limit implanted arrays to tens of electrodes in small animals covering a relatively small area.

Emerging new technologies for recording subdural electrical potentials [micro-electrocortigraphical (μECoG)] could in theory accommodate the above application problem. However, to scale surface arrays to hundreds of electrodes, conventional electrode designs require extremely fine pitch wires, which are not reliably reproducible. Furthermore, as the number of wires increases, chronic implantation becomes increasingly difficult, if not impossible, due to the size, weight and bulk of the connectors and wiring. In principle, multiplexed electrode arrays can scale to higher channel counts with only a small increase in the number of required interface wires.

* M. A. Escabí and H. L. Read contributed equally to this work.

Address for reprint requests and other correspondence: Y. E. Cohen, Dept. of Otorhinolaryngology, Perelman School of Medicine, Univ. of Pennsylvania, 3400 Spruce-5 Ravdin, Philadelphia, PA 19104 (e-mail: ycohen@mail.med.upenn.edu).

Table 1. *Comparison of prior μECoG and μECoG investigations of auditory cortex*

Study	Electrode Type	No. of Electrodes	No. of Wires	Cortical Surface Resolution, μm	Approximate Sampled Cortical Area
Ogawa et al. 2011	Penetrating	64	64	450	2 mm × 1 mm
Takahashi et al. 2003	Surface μECoG	69	69	250	2 mm × 2 mm
Owens et al. 1995	Surface μECoG	25	25	210	1 mm × 1 mm
Besle et al. 2011	Surface μECoG	127	127	10,000	Up to 127 cm^2
Pasley et al. 2012	Surface μECoG	64	64	4,000	10 cm^2
Present study	Surface μECoG	196	29	250	3.5 mm × 3.5 mm

μECoG, micro-electrocortigraphical.

Here, we validated and demonstrated the utility of a new flexible, multiplexed electrode array that enables practical interfaces with hundreds to potentially thousands of electrodes using a small number of external connections, feasible for chronic implantation. Configuration differences between our custom active, multiplexed electrode μECoG array and comparable arrays used previously are summarized in Table 1. Prior studies have exclusively used passive electrodes, with limited numbers of electrodes (<100) and limited cortical area coverage (<4 mm^2). In contrast, this custom active electrode array was designed to record μECoG potentials with fine pitch spacing (250 μm) and large area coverage (12.3 mm^2) in a design that can be readily scaled to cover larger areas. This array provides similar cortical area coverage with higher spatial resolution mapping than our laboratory's previously demonstrated devices (Viventi et al. 2011).

This improvement was enabled by a novel flexible transistor design (Fig. 1*A*, *first* panel). Importantly, by integrating active circuitry directly into the subdural array, we were able to buffer and multiplex the signal outputs, which improved the signal quality and dramatically reduced the number of required interface wires: in this work, we interfaced 196 electrodes using only 29 wires. This small number of wires will be critical for future applications, including

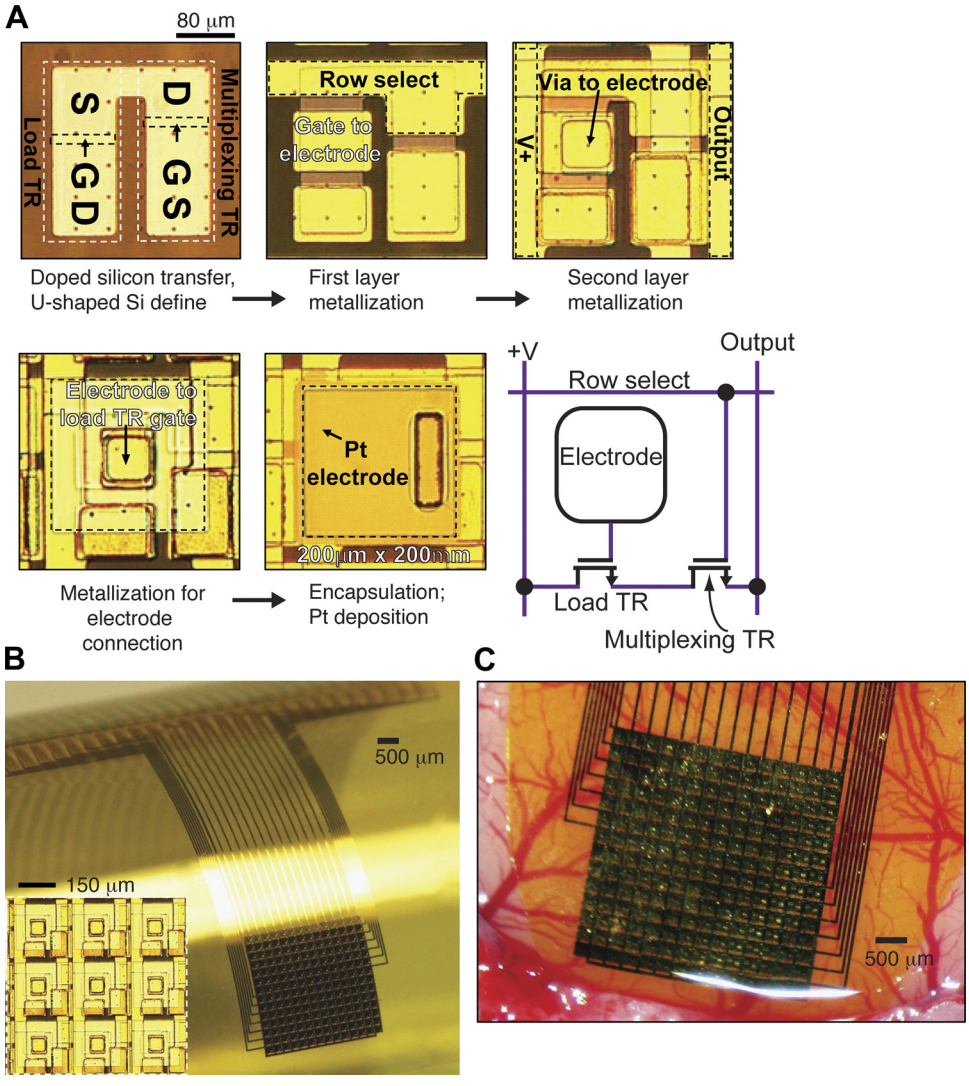

Fig. 1. Micro-electrocortigraphical (μECoG) recording array and technical details of electrode array fabrication. *A*: microscope images of the fabrication process at each layer. *Top left*: "U"-shaped silicon nanoribbons transfer-printed to the flexible polyimide substrate are shown. *Top middle*: the first metal layer provided horizontal row select signals, connections to upper layers for the electrode input, and source/drain contacts. *Top right*: the second metal layer provided connections for the common power wire and shared column output line. *Bottom left* and *bottom middle*: subsequent metal layers and encapsulation layers provided connection between the surface electrodes and the load transistor (Tr) as well as protection for the active circuit elements from biological fluids. *Bottom middle*: lastly, a final encapsulation layer and Pt electrode deposition step finalizes the device. *Bottom right*: schematic circuit diagram of a single unit-cell containing two matched Tr. *B*: the 14 × 14 organization of the electrodes in the μECoG recording array. The *inset* shows a magnified view of a 3 × 3 region of the array. *C*: the recording array on the lateral surface of a rat's brain is shown. Pt, platinum.

chronic implantation and recording from high-resolution arrays in freely behaving animals.

Current methodologies fail to record continuous cortical responses with a high degree of spatial and temporal resolution over a large cortical surface area; thus here we explore the possibility that μECoG recording technologies can fill this methodological gap. Fourier intrinsic optical imaging (IOI) methodologies successfully measure metabolic responses to tones with a high degree of spatial resolution across a large cortical area; however, due to the slow time course of the metabolic response, IOI is not ideal for measuring cortical responses with high stimulus evoked timing precision (Kalatsky et al. 2005; Kalatsky and Stryker 2003). Furthermore, despite its high spatial resolution, data acquisition for IOI is relatively slow, requiring tens of minutes to generate cortical response maps. Six tonotopically organized auditory cortical fields have been identified with IOI in the rat temporal cortex (Kalatsky et al. 2005; Polley et al. 2007). Metabolic and spike rate-based tone-frequency responses obtained with IOI and penetrating electrode multiunit recordings are correlated and have a similar spatial resolution for topographic organization (i.e., tonotopy) (Kalatsky et al. 2005; Storace et al. 2011). In the present study, utilizing our custom μECoG array, we find average pure-tone evoked μECoG responses are correlated with IOI pure-tone responses, and the two methodologies yield similar response spatial resolution and tonotopies in multiple rat auditory cortical fields. Furthermore, we demonstrate that the tonotopic organization can be measured quickly at high spatial resolution, with as little as 13.5 s of data acquisition time.

Primary (A1) and ventral nonprimary auditory cortical fields have unique ascending glutamatergic pathways that could alter the timing precision of their responses to dynamic sounds (Storace et al. 2012). Here, we used active μECoG array to record continuous cortical responses to dynamically modulated sounds and demonstrated novel differences in response timing precision in A1 vs. ventral nonprimary auditory cortical fields of the rat. Temporally precise responses of auditory pathway neurons can be quantified by playing continuous 10-min-long segments of dynamic moving ripple (DMR) noise sounds and reconstructing the spectrotemporal response field (STRF) (Escabi and Read 2005). A similar approach has been used to record STRFs in A1 of rodents previously (Geffen et al. 2011; Linden et al. 2003; Machens et al. 2004). This approach also has been adapted to quantify temporally precise A1 local field potential responses with μECoG arrays (Owens et al. 1995; Takahashi et al. 2003). Here, we assess temporally precise and reliable μECoG STRFs in A1, ventral auditory field (VAF), and a region dorsal to A1. Significant STRFs were obtained with μECoG in A1 and the region dorsal to A1, indicating a high degree of temporally precise (synchronized) responses to DMR. In contrast, few significant STRFs were evident in VAF. Thus there is a higher timing precision of responses in A1 than VAF as predicted based on glutamateric pathway differences. These findings suggest that this new μECoG array technology has the potential for large-scale, temporally precise continuous monitoring and functional mapping of sound responses in multiple cortical fields, without the use of invasive penetrating electrodes.

MATERIALS AND METHODS

Animals and Surgical Procedures

Surgeries and brain recordings were carried out in a total of six adult male rats (Brown Norwegian). Responses were recorded with our custom active μECoG array in three of these rats and with a commercially available passive μECoG array (NeuroNexus Technologies, Ann Arbor, MI) in the remaining three animals. Anesthesia was induced with a cocktail of ketamine (12–60 mg/kg), xylazine (1.25–7 mg/kg), and acepromazine (0.25–0.5 mg/kg) and was maintained in a stage III, plane II of general anesthesia with pentobarbital sodium (20–50 mg/kg intraperitoneally) for surgical and experimental procedures. Anesthesia was supplemented as needed to maintain areflexia, and anesthetic depth was monitored periodically via pedal reflex and heart rate (electrocardiogram; GE Healthcare, Waukesha, WI). Once the rats were anesthetized, we performed a tracheotomy and cisterna-magnum puncture. To minimize respiratory secretions and cerebral edema, respectively, atropine sulfate (0.1 mg/kg) and dexamethasone (0.25 mg/kg) were administered. The skull and dura were removed to expose the temporal cortex in the right cerebral hemisphere. For the intrinsic optical-imaging studies, the exposed brain was covered with agar and sealed with a glass coverslip. Following the imaging studies, the coverslip and agar were removed, and the μECoG electrode array was placed directly on the cortical surface. All housing and experimental procedures were done according to the approved guidelines of the Institutional Animal Care And Use Committee at the University of Connecticut and in accordance with National Institutes of Health and American Veterinary Medical Association guidelines.

Auditory-Stimulus Delivery and Design

Auditory stimuli were delivered binaurally with a closed calibrated audio system. The stimuli were generated off-line with custom C^{++} or MATLAB (The Mathworks) software at a rate of 98 kHz or 96 kHz, 24-bit resolution, and delivered with a dynamic drive (Beyer DT 880, custom housing). The closed-speaker system was calibrated at the rat's ear with a 400-sample finite-impulse response inverse filter that was implemented on a RX6 multifunction processor (Tucker-Davis Technologies). The close-field system was linear (input-output coherence >0.95) and had a flat frequency response between 1 and 47 kHz (± 3 dB). During the μECoG-array recordings, auditory stimuli were delivered at 96 kHz with a DIGI 9652 (RME) professional audio card connected optically to an ADI-8 DS digital-to-analog converter (RME). When the optical-imaging data were collected, auditory stimuli were delivered with a Lynx Studio Technology audio card at 98 kHz.

Auditory Stimuli

To assess tone responses with IOI, auditory stimuli delivered included 16 pure-tone pips (5-ms rise time, 50-ms duration, a 250-ms intertone interval). All tones were presented at a single sound level [45 dB, sound pressure level (SPL)]. Pure-tone pip sequences were presented as ascending (2–32 kHz) or descending (32–2 kHz) (0.25-octave steps) sequences that repeated for continuous acquisition of IOIs. The responses from the pure-tone stimuli were used to calculate the best frequency (BF; see below).

To assess pure-tone responses with μECoG potentials, auditory stimuli delivered included pure-tone pips (5-ms rise time, 50-ms duration). Tone pip frequency and sound level were varied between 1.4 and 45 kHz (⅛-octave steps) and 5 and 85 dB SPL (10-dB steps), respectively. Each frequency and level combination was delivered six times in a random interleaved order at a rate of 3.3 Hz (300-ms intertone interval). The responses from the tone-pip stimuli were used to calculate the frequency response area (FRA), BF, and bandwidth (BW, see below).

To assess μECoG STRFs, the auditory stimulus was a continuous (10-min duration) DMR noise (Escabí and Schreiner 2002). The DMR was generated digitally at a sampling rate of 96 kHz with 24-bit resolution in MATLAB. The DMR was a continuous time-varying broadband sound that covered the frequency range between 1 and 48 kHz. At any instant of time, the DMR had a sinusoidal spectrum; the density of the spectral peaks was determined by the spectral-modulation frequency (0–4 cycles/octave). The peak-to-peak amplitude of the ripple was 30 dB. The DMR also contained temporal modulations that were controlled by varying the temporal-modulation frequency (0–25 Hz). Both the spectral and temporal parameters varied randomly and dynamically; the maximum rate of change for these parameters was 0.25 Hz and 1 Hz, respectively. This variability in the spectral and temporal properties provided an opportunity to probe the temporal and spectral acoustic space in an unbiased manner. DMR was delivered binaurally at 80 dB SPL (65 dB spectrum level per ⅓ octave), twice (20 min total) during each recording session.

Brain Recordings

Below, we discuss *1*) the construction of and recording methodology for our "active" multiplexed μECoG array; *2*) the recording methodology for a conventional technology "passive" NeuroNexus μECoG array; and *3*) the recording techniques for the IOI.

Active μECoG array. To enable a high-resolution interface with large areas of the rodent brain, we developed an array of cortical-surface electrodes using flexible silicon electronics technology (Fig. 1). Active electrode arrays were fabricated using a multilayer process (Fig. 1*A*). Doped silicon nano-ribbons (~260 nm) were located in the first layer through the use of transfer-printing technology. The array was composed of 392 silicon nanomembrane transistors. A unique "u-shaped" silicon nanomembrane (Fig. 1*A*, first panel) allowed the source of the buffer transistor to be connected to the drain of the multiplexing transistor through a continuous doped region, without using the metal layers above. This enabled the row-select signal (Fig. 1*A*, first layer metal) to pass over the oxide-insulated source and drain regions. Because this u-shape efficiently used the available space, we could design an electrode that had a dense packing of electrodes (Fig. 1*B*, *inset*), while maintaining large feature sizes that were easier to fabricate. The active matrix circuit design contained two transistors per unit-cell (Fig. 1*A*, *bottom right*). The buffer transistor, which was connected to the electrode, buffered the μECoG signals. The multiplexing transistor allowed all of the electrodes in the same column to share a single output wire (Fig. 1*A*, second layer metal). Flexible transistors were fabricated using high-quality single-crystal silicon, enabling high-speed multiplexing (<5 μs) and sampling rates (>10 kS/s) (Viventi et al. 2010) and very low multiplexer cross talk (less than −65 dB) (Viventi et al. 2011).

Subsequent horizontal and vertical metal interconnect layers were insulated using layers of polyimide (~1.2 μm, Sigma Aldrich). Additional polymeric encapsulation layers (Fig. 1*A*, metallization for electrode connection; polymide and epoxy, ~1.2 μm and ~4 μm) with an offset vertical interconnect-access structure prevented electrical-leakage currents when the device was immersed in highly conductive media. As a final step, platinum (~50 nm) was evaporated and deposited onto the electrodes' surface to reduce their impedance (Fig. 1*A*, encapsulation and Pt deposition) (~45 kΩ at 1 kHz). Detailed fabrication procedures have been described previously (Viventi et al. 2010, 2011).

We manufactured a μECoG-recording array with 196 electrodes that were organized into a 14 × 14 matrix (Fig. 1, *B* and *C*). Each surface electrode was 200 × 200 μm, with 50-μm spacing between each recording site, yielding a center-to-center distance of 250 μm. The total size of the recording area was ~3.5 × 3.5 mm. The overall thickness of the multilayer structure composing the electrode array was ~25 μm. Using multiplexing circuitry, each recording site was sampled discretely; the 196-channel recording array required only 29 interface wires. These wires were connected to a custom data acquisition system (Viventi et al. 2011) through a flexible anisotropic conductive film (Elform).

The multiplexed analog signals from the μECoG array were synchronously sampled at 125 kS/s using a custom data-acquisition system (Viventi et al. 2010, 2011) with four data-acquisition cards (PXI-6289, National Instruments). Neural (voltage) signals were recorded relative to a reference electrode that was attached to each animal.

To reduce the recording noise, multiple samples ($n = 30$) were collected and averaged at each recording (electrode) site before sampling μECoG activity at the next recording site. The 14 row select signals of the multiplexed electrode array were cycled at ~8.928 kHz to sample all of the electrodes on the array, yielding an effective sampling rate of ~297.6 Hz per active electrode. All of the 14 electrodes in a given column were sampled sequentially. The multiplexer output settled in less than 5 μs. With improvements in the design of our data acquisition system, the multiplexing rate could be increased to enable sampling rates higher than 14 kS/s per electrode. Here, data were acquired, demultiplexed, filtered (analog high-pass filter at 0.007 Hz), stored, and displayed in real-time using custom LabVIEW software (National Instruments).

Custom passive μECoG array. In three separate animals, we recorded neural activity with commercially available passive μECoG arrays (NeuroNexus; E32-300-20-50). Unlike the active transistor μECoG arrays designed here, the NeuroNexus is a passive μECoG array containing 32 electrodes arranged into 4 columns and 8 rows with 300-μm contact spacing and contact diameter of 50 μm (1,963-μm contact area). Neural data were acquired for these arrays with a TDT Z-series system (PZ2–128 amplifier and RZ2 processor) at a sampling rate of 2 kHz. Note that the custom array covers a larger area, with higher spatial resolution, and a larger number of electrodes than the commercially available array used in this study. This will impact on extent and possibly resolution of response topographies. Hence, site-by-site comparisons are made between IOI and array responses in the RESULTS section.

IOI. A1 and secondary auditory cortical fields differ in average sound-response properties and the topography of these response properties as demonstrated with multiunit penetrating electrode and IOI methodologies (Funamizu et al. 2013; Higgins et al. 2010; Kalatsky et al. 2005; Polley et al. 2007; Storace et al. 2011). Tone responses obtained with IOI and multiunit penetrating electrodes are correlated and have similar tonotopic organization (Escabi et al. 2007; Kalatsky et al. 2005; Storace et al. 2011). Here, IOI was used as it provides a larger area of response acquisition coverage in a shorter amount of time than penetrating electrode arrays. Fourier methods were used to extract the phase and magnitude of the intrinsic metabolic response to continuous (and periodic) auditory stimuli, as described in detail elsewhere (Kalatsky et al. 2005). After preparing a rat and positioning the earbars and speakers, a Dalsa 1M30 CCD camera (512 × 512 pixel array) was focused on the cortical surface. The cortex was illuminated with green-wavelength (547 ± 10 nm) light to obtain a 4.6 × 4.6 mm^2 image of the surface blood vessels. Next, the focal plane was translated down by 650 μm, and the reflectance of red-wavelength light (605 ± 10 nm) was recorded while diotically presenting the tone sequences. Because ascending and descending tone sequences yielded similar IOI frequency topographies, the hemodynamic delay was corrected by subtracting the ascending and descending maps to create a frequency difference tone-response map (Higgins et al. 2010; Kalatsky et al. 2005). To reduce the pixel variability, tone-response maps were Gaussian filtered (SD = 162 μm), as described previously (Storace et al. 2011). Note that tone-responses obtained with IOI were at a single binaurally matched low sound level (45 dB SPL). Using this high correlation between the multiunit BFs and IOI BFs is obtained whether considering unit-response BF estimates from a single matched SPL or from

the entire unit-response FRA (Higgins et al. 2008; Kalatsky et al. 2005; Storace et al. 2011).

Data Analysis

Calculating BF and BW from μECoG FRA. FRAs were computed from the continuous μECoG data. We collected μECoG data while tone pips, which varied in frequency and sound level, were delivered to a rat. For each recording site, we computed the average response to each tone-pip across six trials over a window of 300 ms following tone-pip onset. The FRA was obtained by calculating the average peak-to-peak voltage value as a function of tone frequency and sound level.

For each recording site, a FRA was significant if the FRA-data samples exceeded a significance criterion of $P < 0.001$. Samples that did not meet this significance requirement were set to a value of zero. As a null hypothesis, we assumed that the μECoG signal had equal power but occurred randomly with respect to the tone pips. We simulated this scenario by creating a random "noise" FRA (nFRA). This nFRA was created by first randomizing the μECoG signal's phase spectrum. This phase randomization preserved the power spectrum of the original signal and thus generated a noise response that was temporally uncorrelated with the tone pips. Next, the nFRA was computed as described above for the original data. This procedure was bootstrapped (50 iterations), and the samples from the nFRAs formed a reference-noise distribution. Because nFRA samples were normally distributed (χ^2 test, $P < 0.01$), we required that the original FRA samples exceeded 3 SDs of the nFRA to achieve a significance level of $P < 0.001$. Using only those significant FRA samples, a recording site's BF was defined as the center-of-mass of the FRA at 65 dB SPL. This sound level was chosen because significant responses could be measured across the majority of recording sites of the array at this SPL. The BW of the tone FRA was measured as twice the SD of tone-frequency response at 65, 75, or 85 dB SPL.

Determining cortical field boundaries and calculating BF from the intrinsic optical image. The pure-tone BF estimates from the IOI were obtained as described in detail previously (Higgins et al. 2010; Storace et al. 2011). Here, the pure-tone BFs estimated from IOI and μECoG array recordings were compared for data from the same cortical site measured with each method. Our optical images were obtained at a sound level of 45 dB, whereas μECoG data were analyzed at a sound level of 65 dB. This was done because many of the cortical sites did not exhibit statistically significant responses with μECoG at 45 dB SPL, and thus BFs could not be obtained to compare against the IOI. Consequently, there is a 20-dB difference in the sound level of the tones used to estimate BF for the two methodologies. This is a reasonable comparison, as our laboratory's prior studies found minimal differences in BFs between 45 and 75 dB in A1 (Higgins et al. 2008). Likewise, BFs estimated from a single sound level in the IOI are highly correlated with BFs estimated from the average of several sound levels (Kalatsky et al. 2005). The cortical field boundaries between A1, VAF, anterior (AAF), and suprarhinal auditory fields (SRAF) were determined by the direction of the BF gradients in the IOI, as described in detail elsewhere (Higgins et al. 2010) and by others (Doron et al. 2002; Kalatsky et al. 2005; Rutkowski et al. 2003; Takahashi et al. 2011). The active μECoG array covered A1, VAF and AAF, whereas the passive μECoG array covered a smaller area excluding AAF in some animals. Hence, detailed comparisons between IOI and μECoG estimates of BF were made for those locations that overlapped with both recording methodologies.

Calculating and identifying reliable STRFs with the active μECoG array. Additionally, for our activity μECoG array, we generated the STRFs at each electrode site. Specifically, for each electrode site, a STRF (558 frequency × 151 temporal samples) was computed from the continuous μECoG signal that was collected while the DMR stimulus was delivered to a rat. Because the auditory stimulus and the μECoG signal were continuous, the STRF was generated by cross-correlating the stimulus' spectrotemporal envelope [STRF (τ, X_k)] with the μECoG signal [$r(t)$]:

$$\mathrm{STRF}(\tau, X_k) = \frac{1}{\sigma_S^2}\langle r(t+\tau) \cdot S(t, X_k)\rangle \quad (1)$$

where $\langle\cdot\rangle$ is the time-average operator, X_k is the octave frequency of the kth frequency channel, and σ_S^2 is the variance of the DMR spectrotemporal envelope.

For each recording site, we identified statistically significant spectrotemporal samples of the STRF that exceeded a significance criterion of $P < 0.001$. As a null hypothesis, we assumed that the μECoG signal occurred randomly with respect to the DMR stimulus. We simulated this scenario by creating a random "noise" STRF (nSTRF). This nSTRF was generated by first randomizing the μECoG signal's phase spectrum. The resulting signal's power spectrum was identical to the original μECoG signal but had a random temporal response. Next, we cross-correlated this phase-randomized signal with the stimulus' spectrotemporal envelope (using *Eq. 1*). This procedure was bootstrapped (50 iterations), and the samples for each of the nSTRFs formed a reference-noise distribution. Because the nSTRF samples were normally distributed (χ^2 test, $P < 0.01$), we required that the original STRF samples exceed 3 SDs of the nSTRF to achieve a significance level of $P < 0.001$.

For any given trial of the DMR, ~84 STRF samples (151 temporal × 558 spectral samples × 0.001 = 84.3 samples) were false positives; that is, they exceeded the significance level of $P < 0.001$ by chance. Whereas such samples exceeded the significance criterion, they did not satisfy the primary objective of identifying STRFs that had reproducible auditory responses. To overcome this issue, we computed a "reliability" index (RI) that identified STRF samples with significantly reproducible structure. The RI was calculated by first segmenting the continuous μECoG response into 60-s-long segments (20 segments total). One-half of the 60-s segments were selected at random, and two STRFs were generated with each half of the data ($\mathrm{STRF_A}$ and $\mathrm{STRF_B}$). This procedure was bootstrapped 500 times. For each iteration and as a function of each sample, we computed the correlation coefficient between $\mathrm{STRF_A}$ and $\mathrm{STRF_B}$. RI was defined as the average correlation coefficient across all bootstrap iterations. RI values near 1 indicated that a STRF sample was highly reliable. In contrast, RI values near 0 indicated that the STRF sample was not reliable. Finally, a recording site was defined to contain a "significant response" only if the RI exceeded chance reliability. To calculate this probability, the RI was first calculated from the phase-randomized μECoG signal. Using the distribution of RI measurements obtained for this phase-randomized μECoG, reliable sites were identified at a significance level of $P < 0.01$. Only those recording sites that contained a significantly reliable response were considered for further analysis.

ESTIMATING STRF PARAMETERS. The preferred spectral and temporal modulation of a recording site was estimated from the ripple-transfer function, which was the two-dimensional Fourier transform of a significant STRF. The spectral- and temporal-modulation transfer functions were calculated by *1*) collapsing the ripple-transfer function relative to its spectral and temporal dimensions, respectively, and *2*) then normalizing each function for a maximum gain of one. The "best" spectral and temporal modulations were the center-of-mass values of these respective functions. The spectral-modulation upper-cutoff frequency was the modulation frequency where the gain of the spectral-modulation function was reduced by 3 dB (or equivalently to 50% of the maximum power). The temporal-modulation upper-cutoff frequency was defined in an analogous manner. Details of the ripple transfer-function analysis have been reported previously (Qiu et al. 2003; Rodriguez et al. 2010b).

Other response parameters were also measured directly from each recording site's STRF. The BF and "response delay" were defined, respectively, as the frequency and temporal lag that corresponded to

the maximum STRF value. Note that the STRF BF and the pure-tone BF: *1*) are generated from DMR and pure-tone auditory stimuli, respectively, and *2*) they are potentially different in that they reflect temporally precise phase-locked activity to the DMR for the STRF vs. the maximum firing rate to tones from the FRA, respectively. We also estimated the BW and integration time of each STRF to characterize the spectral and temporal resolution of each recording site. To estimate these values, we first obtained a response time-frequency power distribution by computing the squared magnitude of the Hilbert transform of each STRF. Next, the spectral- and temporal-marginal functions were calculated by collapsing this power distribution along its spectral and temporal dimensions, respectively. The STRF "bandwidth" was twice the SD of the spectral-marginal function, and the STRF "integration time" was twice the standard deviation of the temporal-marginal function (Rodriguez et al. 2010b).

Correlation between recording sites on the active μECoG array. The correlation between two recording sites on the active μECoG array was calculated by finding the cross-correlogram between the concatenated μECoG signals that were elicited over the combined first and second 10-min representations of the DMR stimulus (20 min total). Given the measured neural response from sites k [$s_k(t)$] and l [$s_l(t)$], the cross-correlation was first obtained as

$$r_{kl}(\tau) = \frac{1}{T}\int_T \left[S_K(t) - \mu_k\right]\left[S_1(t+\tau) - \mu_1\right]\mathrm{d}t$$

where μ_k and μ_l are the mean values of the response. The normalized correlation was then defined as

$$\mathrm{C}_{Kl}(\tau) = \frac{\varphi_{kl}(\tau)}{\sigma_k \sigma_l}$$

Note that the cross-correlations (i.e., correlations between μECoG signals at different sites) reflected contributions of both signal and noise correlations (i.e., neural variability, etc.). If the measured neural responses contain both a sound-driven [signal, $x(t)$] and neural variability [noise, $n(t)$]:

$$S_K(t) = X_k(t) + n_k(t)$$

and the signal and noise are independent, it can be shown that:

$$\mathrm{C}_{Kl}(\tau) = \frac{\varphi_{x_k x_1}(\tau)}{\sigma_k \sigma_l} + \frac{\varphi_{n_k n_1}(\tau)}{\sigma_k \sigma_l} = \mathrm{C}_{kl}^{\mathrm{signal}}(\tau) + \mathrm{C}_{kl}^{\mathrm{noise}}(\tau)$$

Thus the normalized cross-correlation, in general, reflects both signal and noise correlations from the measured response.

The significance of the correlation was calculated with a bootstrap analysis: we independently randomized the phase of two μECoG signals, which maintained their magnitude spectrum, and then calculated the correlation between these randomized signals. This process was repeated 5,000 times to generate a distribution of correlation values that we compared with the actual peak-correlation value. Further analysis was restricted only to those sites with significant ($P < 0.01$, relative to the randomized distribution) peak-correlation values. We also limited our analyses to cross-correlograms with peaks occurring at times ≤0.1 s, which are typical of those found in studies of single-unit cross-correlation (Miller et al. 2001), and to pairs of sites that had significant STRFs.

RESULTS

FRAs Generated with a Custom Active μECoG Array

To quantify the frequency selectivity of a recording site, FRAs were generated on each electrode in the array by measuring the cortical μECoG response to tone pips of varying frequency and sound levels (6 repetitions per condition, MATERIALS AND METHODS). The spatial distribution of FRAs from six trial-averaged μECoG responses from one animal is shown in Figure 2.

To illustrate the reliability of the responses from our custom active μECoG array, Fig. 3 compares single-trial responses with trial-averaged responses from a single recording site. The top panels in this figure show the single-trial μECoG response traces (Fig. 3*A*) and the trial-averaged (Fig. 3*B*) μECoG responses. Individual and trial-averaged responses were typically biphasic, resembling in some respects local field responses to a variety of sounds in rat auditory cortex (Centanni et al. 2014; Reimer et al. 2011; von der Behrens et al. 2009). The *bottom* panels show the single-trial FRA and the corresponding trial-averaged FRA. As can be seen, the selectivity and sensitivity of the single-trial FRA was comparable to that generated from the trial-averaged responses, although more variable. Indeed, the single-trial FRA had a "v-shaped" tuning profile that is characteristic of FRAs that are generated through single-unit and multiunit recordings and other techniques in A1 (Pickles 1988; Polley et al. 2007; Storace et al. 2010). Three additional six-trial FRAs (Fig. 4, *A–C*) and their corresponding single trial-averaged FRAs (Fig. 4, *D–F*) show the same relationship.

Next, we compared the cortical position maps and values for BFs obtained from single- vs. six-trial-average FRAs. We calculated BF from each statistically significant FRA (see MATERIALS AND METHODS), where BF was defined as the center of mass of the FRA at a given SPL (e.g., 65 dB). BF maps were generated by plotting the measured BF as a function of each electrode site's center location. As shown, there is a high correspondence between single-trial (Fig. 4*G*) and six-trial-averaged BF maps (Fig. 4*H*). Indeed, when we plotted, on a site-by-site basis, the trial-averaged BF against the single-trial BF, we found that they were highly correlated (Fig. 4*I*; $r = 0.95 \pm 0.01$, mean ± SE; average of all cases, $r = 0.92 \pm 0.02$, mean ± SE). Thus frequency organization can be quickly and accurately derived with the active μECoG array with as little as one response trial with a 13.5-s total acquisition time to probe responses to 45 frequencies at 1 sound level with an interstimulus interval of 300 ms.

A Comparison Between the Frequency Organization of the Auditory Cortex as Assessed with μECoG Arrays, and IOI

An orderly spatial organization and correspondence is observed between multiunit and IOI metrics of BF responses to tone pips (Kalatsky et al. 2005; Polley et al. 2007). Here, we examined whether a similar correspondence existed between IOI- and active μECoG-derived responses; we chose to compare array activity with Fourier optical-imaging data because, like the μECoG-array data, it facilitates simultaneous observation across large regions of cortex and is a "gold" standard technique for large-scale recordings of neural response related activity (Higgins et al. 2010; Kalatsky et al. 2005).

IOI and active-μECoG-array activity were recorded from the same cortical positions. The IOI, the surface vasculature, and the corresponding locations of the electrode sites of the custom active μECoG array (dots) are illustrated for one animal (Fig. 5*A*). Figure 5*A* shows the spatial distribution of IOI BF over a large region (4.6 mm × 4.6 mm) of the auditory cortex that included three tone-frequency response minima (Fig. 5*A*, "Low") and BF gradient reversal between A1 and

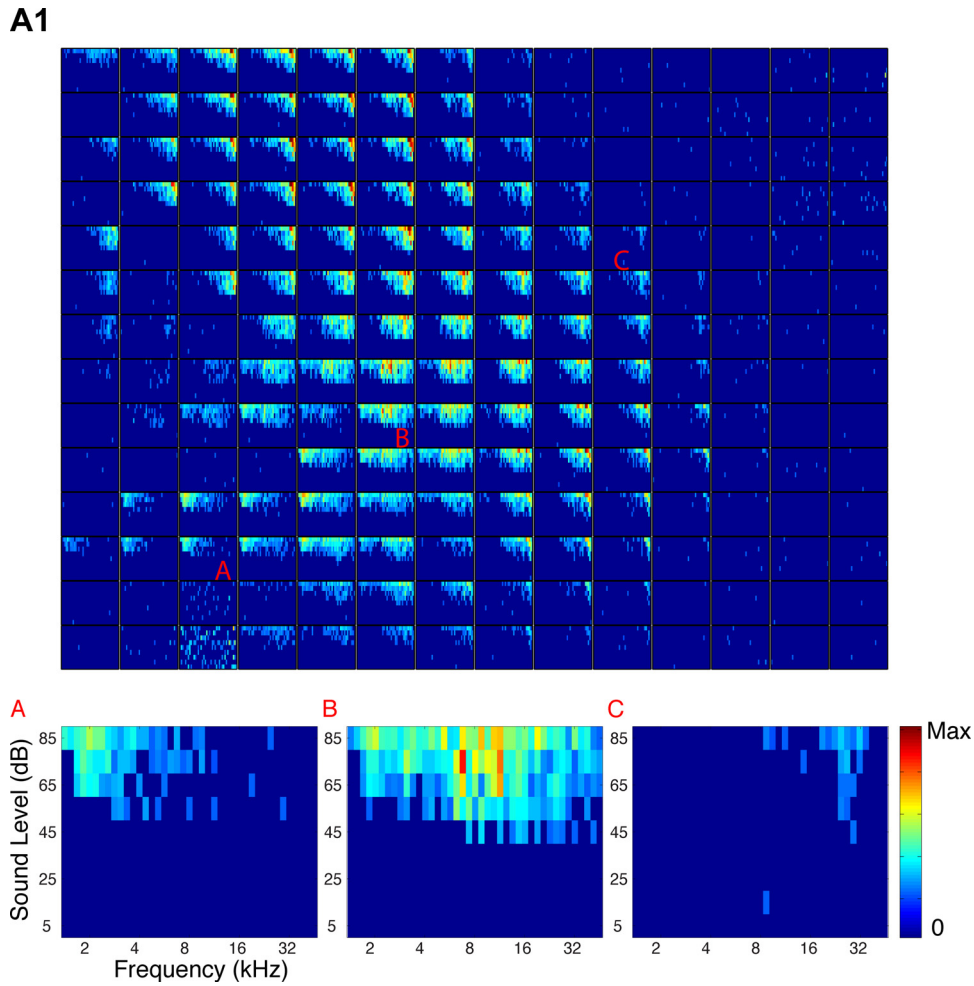

Fig. 2. Topographic distribution of frequency response areas (FRAs) derived from μECoG activity. *A1*: topographic organization of the FRAs generated from each recording site on the array. Each square demarcates the relative location of each electrode and the FRA generated from the neural activity recorded at that site. For each FRA, frequency in kHz is plotted on the *x*-axis, and sound pressure level (SPL; dB) is plotted on the *y*-axis. Red regions indicate frequency-sound level combinations that elicited neural activity that was above baseline activity; see color bar. Note that all of the FRAs are normalized relative to the site with the maximum response using a common scale as the number of SDs above the baseline voltage of each recording site. Blue regions indicate frequency-sound level combinations that elicited neural activity that was at or near the baseline. *A*, *B*, and *C*: three FRAs were selected to illustrate the variability in tuning properties observed with the μECoG array. The respective panel letter denotes the topographic location of each of these FRA within the μECoG array (*A1*). SD, standard deviation.

AAF, VAF and SRAF, SRAF and AAF. Recording sites covering AAF (Fig. 5*A*, AAF, white dots) were removed for data analysis, as they were not recorded with μECoG arrays in all animals. The region of interest in auditory cortex included A1, the region dorsal to A1, and VAF, which were defined by the reversals and directions of optical BF gradient, as described previously (Higgins et al. 2010). Figure 5*B* plots BF position map for A1, the area dorsal to A1, and VAF. Figure 5*C* plots the same position map for FRA BF as derived through the custom active μECoG recording array. For both the optical and active μECoG derived data, BFs progressed from low to high along the caudorostral axis in all three tested animals.

Next, we quantified the degree of correspondence between the optical and μECoG FRA BFs. For the example animal shown in Fig. 5, there was a high correspondence between the optical and custom active-μECoG BFs (Fig. 5*D*; optical BF vs. active μECoG BF: $r = 0.73 \pm 0.06$, $P < 0.05$). There was also a significant correlation when we considered all three tested animals (optical BF vs. μECoG BF: $r = 0.64 \pm 0.04$, $P < 0.05$).

In three additional animals, we recorded IOI and μECoG responses with conventional passive electrode arrays (NeuroNexus) to compare responses to those derived from our custom active μECoG arrays. Figure 6*A* is a photograph of the surface vasculature, and the surface positioning of the passive array for one animal. Thirty-two simultaneously recorded six-trial-averaged FRAs obtained from the array in this animal are shown (Fig. 6*B*). Like our custom active μECoG array (Figs. 3 and 4), many of these FRAs had a characteristic v-shaped tuning profile (Pickles 1988; Polley et al. 2007; Storace et al. 2010).

An overlay of an IOI, surface vasculature and the passive array center positions (Fig. 7*A*) illustrates where BF estimates were obtained in this same animal as shown in Fig. 6. Again, the IOI revealed three frequency-response minima (Fig. 7*A*, "Low") and BF gradient reversals between A1 and AAF, VAF and SRAF, SRAF and AAF. Figure 7*B* plots the position maps of BF estimated from IOI for the region covered by the passive array that included A1, area dorsal to A1 and VAF. Again, we found that BFs progressed from low to high along the caudorostral axis with data from the IOI (Fig. 7*B*) and from the passive array (Fig. 7*C*). IOI and passive μECoG BFs were significantly correlated (Fig. 7*D*; optical BF vs. μECoG BF: $r = 0.60 \pm 0.12$, $P < 0.05$; average across all animals, $r = 0.58 \pm 0.22$).

We found two key differences between our custom active μECoG arrays and the conventional passive arrays as evident by comparing two examples (Figs. 5 and 7). First, unlike our active μECoG arrays in which there was a roughly one-to-one correspondence between the optical BF and the μECoG BF (average difference between the optical and array BFs = 0.03 ± 0.05 octave, $P > 0.05$; e.g., Fig. 5*D*), BFs for the

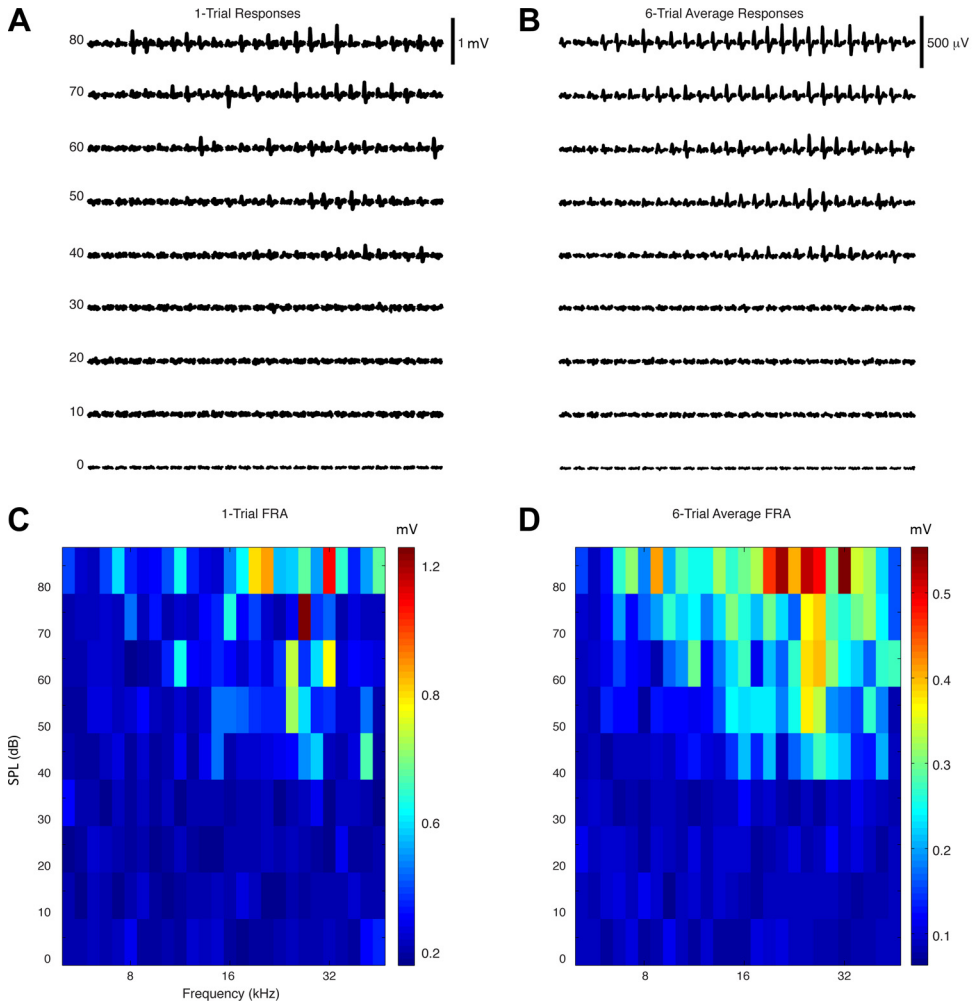

Fig. 3. Reliability of single-trial and trial-averaged μECoG responses from a single electrode site on the active μECoG array. *A*: single-trial μECoG voltage response traces to single tone pips at each frequency (*x*-axis) and sound level (*y*-axis) combination. *B*: trial-averaged μECoG voltage response traces that were generated from six tone pip presentations at each level and frequency combination. Like *A*, these data are organized as a function of frequency (*x*-axis) and sound level (*y*-axis). *C* and *D*: the FRAs generated from the single-trial and trial-averaged μECoG responses, respectively. The color bar indicates measured peak-to-peak voltage from the recorded voltage traces in *A* and *B*.

conventional arrays were positively biased (average difference between the optical and array BFs = 0.2 ± 0.04 octave, $P < 0.01$; e.g., Fig. 7*D*). A second difference we observed was that the active μECoG array represented a continuous full range of BF responses between 2 and 32 kHz, whereas the passive array represented a less continuous (compressed) and truncated range of BFs between 3 and 10 kHz (compare Figs. 5*C* and 7*C*).

Change in Frequency BW with Sound Level

The active-μECoG-array responses were resolved enough to reveal a systematic relationship between BF and BW as described previously for multiunit recordings in auditory cortex. Data from one animal illustrate how the active-μECoG-array BW followed an inverted "U-shaped" BW vs. BF function (Fig. 8), similar to that reported for spike-rate-based FRAs in rat A1 (Funamizu et al. 2013; Miyakawa et al. 2013). The BW organization and BF vs. BW relationship persisted at the two highest average sound levels (75 and 85 dB).

Comparisons between the passive vs. active electrode recordings revealed differences in observed BW range and level dependence. For this comparison, FRAs were selected from AI identified sites, and the data were randomly resampled so that BFs of the active and passive arrays were equally distributed (following a uniform distribution between 2.3 and 16 kHz). FRAs were more narrowly tuned, BWs were less sound-level dependent, and the range of BWs was compressed for the conventional passive (Fig. 9, gray line) vs. custom active μECoG array (Fig. 9, black line). Specifically, across all measured sound levels, the BWs of the custom array FRAs were significantly ($P < 0.001$, rank-sum test) higher than those of the conventional array. Furthermore, the custom μECoG array BWs increased systematically with sound level (Fig. 9, black line), as previously observed with multiunit spike rate responses in auditory cortex (Pickles 1988; Polley et al. 2007; Storace et al. 2010). The conventional array FRAs by comparison were much more level invariant (Fig. 9, gray line). This was true even though the cortical regions and BFs ranges were matched for both arrays (BFs were uniformly distributed between 2.3 and 16 kHz).

Overall, the frequency organization of the auditory cortex can be readily measured with the high-density active μECoG arrays proposed here (Fig. 5), as well as the more conventional passive arrays (Fig. 7). However, only our active μECoG array had a frequency resolution comparable with that of high-resolution IOI and multiunit spike rate recordings. In contrast, the passive conventional array did not yield a veridical representation of tonotopy, and BFs were positively biased, relative to IOI. Furthermore, pas-

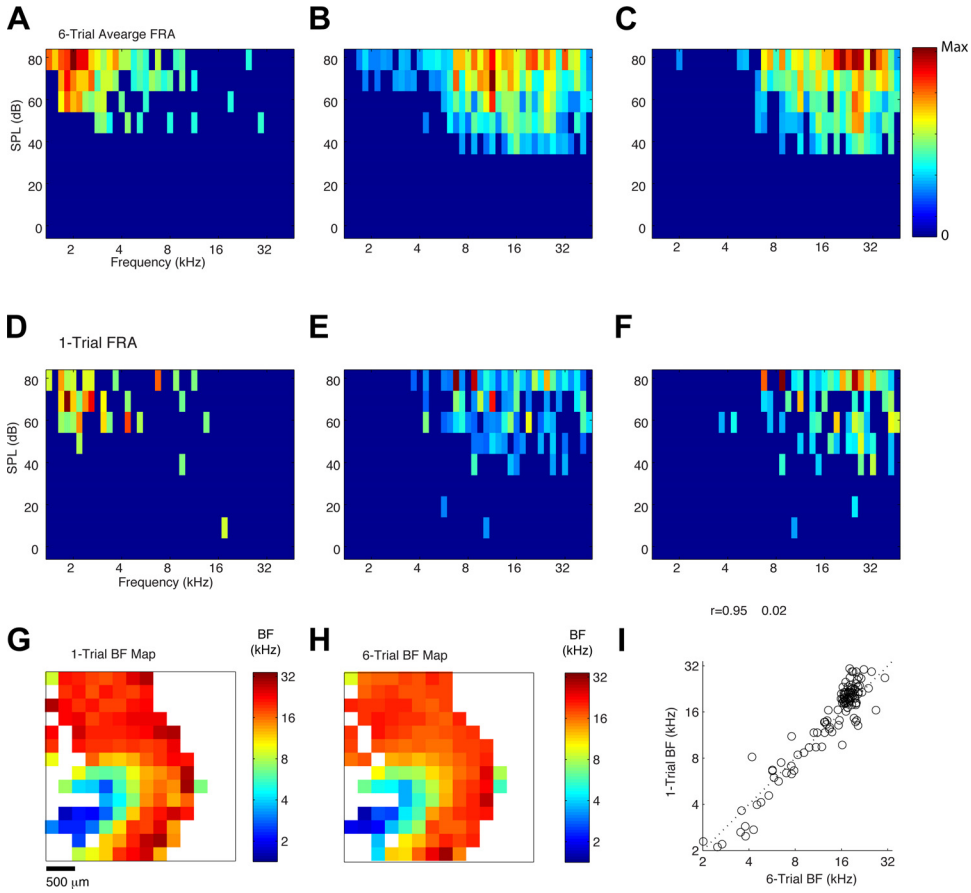

Fig. 4. High correspondence between the best frequencies (BFs) of single-trial FRAs and trial-averaged FRAs. Three examples of single-trial FRAs (*A–C*) are shown with their corresponding trial-averaged FRAs (*D–F*). For these plots, color indicates the maximum peak-to-peak voltage: blue indicates 0 V, and dark red indicates the highest peak-to-peak voltage observed for that particular electrode site. A map of BF that was generated from the single-trial FRA data (trial number 3) at each electrode site is shown in *G*, whereas the trial-averaged map of BF is shown in *H*. The color bar between *G* and *H* indicates the frequency scale (kHz) of these two BF maps. *I*: the site-by-site correlation ($r = 0.95 \pm 0.01$, mean ± SE) between the single-trial BF and the trial-averaged BF for significant FRAs obtained from this animal; the gray line is the line of unity. Data from this same animal are shown in Fig. 8.

sive-μECoG-array BWs were narrower and less level dependent. These differences in the measured neural response organization presumably stem from properties of the array; however, the present study cannot determine the source of such differences conclusively.

Measuring Spectrotemporal Sensitivities with the Active μECoG Array

The μECoG STRF was computed to determine whether our active μECoG array could record the temporally precise, phase-locked responses that are characteristic of single and multiunit responses in A1 (Atencio and Schreiner 2012; Norena et al. 2008). This μECoG STRF was computed to determine what components of the DMR sound drove temporally precise (i.e., phase-locked) surface cortical responses. Each recording site's μECoG-derived STRF was computed by cross-correlating the μECoG-derived signal with the DMR stimulus (see MATERIALS AND METHODS). As seen in Figs. 10 and 11, the μECoG STRFs exhibited an on-off temporal response pattern (Fig. 10*A*, red-blue areas) that is typical of single- and multiunit cortical STRFs, as well as STRFs generated with subdural μECoG arrays (deCharms et al. 1998; DePireux et al. 2001; Eggermont et al. 1981; Escabí and Read 2003; Escabí and Schreiner 2002; Fritz et al. 2003; Linden et al. 2003; Machens et al. 2004; Miller et al. 2002; Pasley et al. 2012).

An exemplar case illustrates the spatial organization of the significant μECoG-derived STRFs (Fig. 10*A*) and their corresponding BF (Fig. 10*B*) and reliability (Fig. 10*C*) indexes. The region corresponding to A1 (Fig. 10, *B* and *C*, black outlined area) has directional components in the caudorostral and ventral-dorsal anatomic axes, as is characteristic of multiunit and IOI responses in A1 (Higgins et al. 2010). In A1, the STRF BFs ranged from 2 to 32 kHz (Fig. 10*C*, black outlined area) and were topographically organized along the same anatomic axis as the tone-evoked BFs measured in the same animal (e.g., Fig. 5, *B* and *C*). Position maps of the reliability and BF indexes indicate that the cortical region dorsal to A1 had the highest STRF reliability and BFs (Fig. 10, *B* and *C*, red areas). This high-BF dominated region was not evident in the tone evoked BF estimated from the IOI (Fig. 5*A*) or the active μECoG (Fig. 5*B*). There were few significant STRFs in the region below A1 corresponding to VAF (Fig. 10*B*, ventral to black outline). In contrast, there were significant tone evoked active μECoG FRAs in VAF in this animal (Figs. 2 and 5*C*). Together, these observations indicate that cortical responses to dynamically modulated sound are temporally precise (and phase-locked) in A1 and in the dorsal area but not in VAF.

As an objective criterion for determining the response reliability, we estimated the significance of each STRF (bootstrap test, $P < 0.001$; see MATERIALS AND METHODS). For the BF data shown in Fig. 10*A*, 38% (75/196) of the recording sites had a STRF with a significant RI ($P < 0.01$; colored squares in Fig. 10*B*) with the most reliable sites clustered on the dorsal aspect of the array. Nonsignificant recording sites (white; Fig. 10*B*) in all areas, including VAF, might have produced change in activity that was not temporally phase-locked with the auditory stimulus.

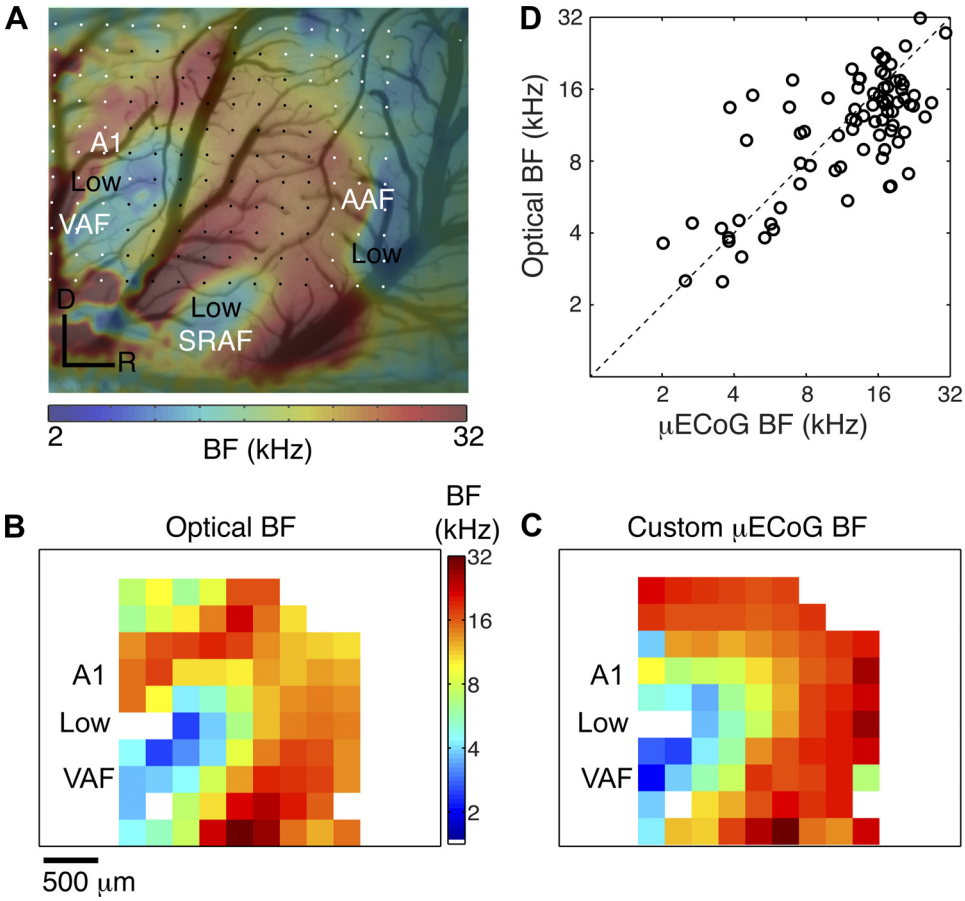

Fig. 5. Correlation between FRAs generated from intrinsic optical imaging (IOI) and custom active-μECoG-array recordings. *A*: composite image of the lateral surface of a rat's brain, including surface vasculature and IOI responses to tone sequences; the color bar indicates the tone BF. The gray and black dots indicate the locations of each electrode of the array: black dots indicate those electrodes that overlapped with the primary auditory cortex plus the area dorsal to primary (A1) (labeled A1) and ventral auditory field (VAF), as defined by IOI. Scale bars indicate 500 μm, dorsal (D) and ventral (V) anatomic axes. *B* and *C*: the BF maps generated from IOI and μECoG FRA data, respectively. The IOI BF was averaged over a spatial region corresponding to the spacing (i.e., 250 × 250 μm) between each recording site of the active μECoG array. The color bars indicate the BF (kHz) of these maps. *D*: a significant (RESULTS) site-by-site correlation between the BF values generated from the μECoG FRA and the IOI is observed. The dotted line is the line of unity. The white areas in *B* and *C* either were recording sites that were not in the area of interest or were sites that did not have statistically reliable BFs. The data shown in this figure are the results from a single animal. Spectrotemporal response field (STRF) and STRF BF data for this same animal are shown in Fig. 10.

Sensitivity and the Spatial Organization of Spectral and Temporal Strf Parameters

Next, we tested several spectrotemporal acoustic features of the μECoG STRF (see MATERIALS AND METHODS for details on how these features were calculated). Two points are apparent from the example STRFs that are shown in Fig. 11. First, some sites were narrowly tuned and responded most robustly to a single frequency (i.e., dark red regions in Fig. 11, *A*, *D*, and *E*). In contrast, other sites were more broadly tuned and responded in a phase-locked manner to multiple discrete frequencies (see multiple red regions in Fig. 11, *B*, *C*, and *F*). Second, almost all of the STRFs had "on-off" profiles (Fig. 11, *A–F*). That is, the μECoG STRFs had inhibitory/suppressive regions (blue regions in Figs. 10*A* and 11, *A–F*) that were temporally delayed with respect to the fast excitation (red regions). Because most STRFs had similar temporal properties, the variability of temporal-modulation sensitivity across the array was relatively small.

Several spectrotemporal features of the STRF were systematically organized within and across the area corresponding to A1 (e.g., Fig. 12). For example, two STRF parameters that varied systematically in the auditory cortex were BW and best-spectral modulation. The STRF BW represents the range of frequencies that produced phase-locked responses to a sound. The best-spectral modulation was a site's preference for the frequency spacing between the peaks and valleys in the sound spectrum (units of cycles/octave). This parameter is analogous to a visual neuron's sensitivity to the spatial frequency of a visual grating. In A1, BW increased and best spectral modulations changed minimally along BF gradient axis (Fig. 12, *A* and *B*, respectively, black outlined area). Summary data from all three animals illustrates systematic variations in spectrotemporal features of the STRF. BF was positively correlated with BW [Fig. 13*A*; $\log_{10}$(BF) vs. $\log_{10}$(BW), $r = 0.83 \pm 0.02$ (mean ± SE), $P < 0.01$]. An inverted "U" relationship was observed for BF vs. BW plotted in octaves (Fig. 13*B*). In contrast, BW was negatively correlated with the best spectral modulation [Fig. 13*C*; $r = -0.64 \pm 0.04$ (mean ± SE), $P < 0.01$]. Sites dorsal to A1 and a few sites ventral to A1 had significant STRFs, narrow BWs and high spectral modulations, consistent with the observation of high BFs in these regions (e.g., Fig. 12, *A* and *B*, sites outside of the black-outlined area).

We found that one temporal feature of the STRFs, in particular, response delay, was also systematically organized. Response delay corresponds to the time of the STRF maximum amplitude. Response delay decreased along the BF gradient axis of A1 (Fig. 12*C*); consequently, BF and delay were negatively correlated [Fig. 13*D*; $r = -0.47 \pm 0.07$ (mean ± SE), $P < 0.01$]. The regions dorsal to A1 had primarily high BFs and short delays. The best-temporal modulation, another temporal feature of the STRF, was a recording site's preferred rate for changes in stimulus power per unit time (Fig. 12*D*). Unlike the other three parameters, there was little variability in this parameter, and we could not identify any systematic spatial organization.

As the BW of a system increases, the integration time should decrease (Dorf and Bishop 1995). Here, we examined whether this principle holds for spectrotemporal features of the cortical STRF. As expected (Fig. 13*E*), the integration time and tem-

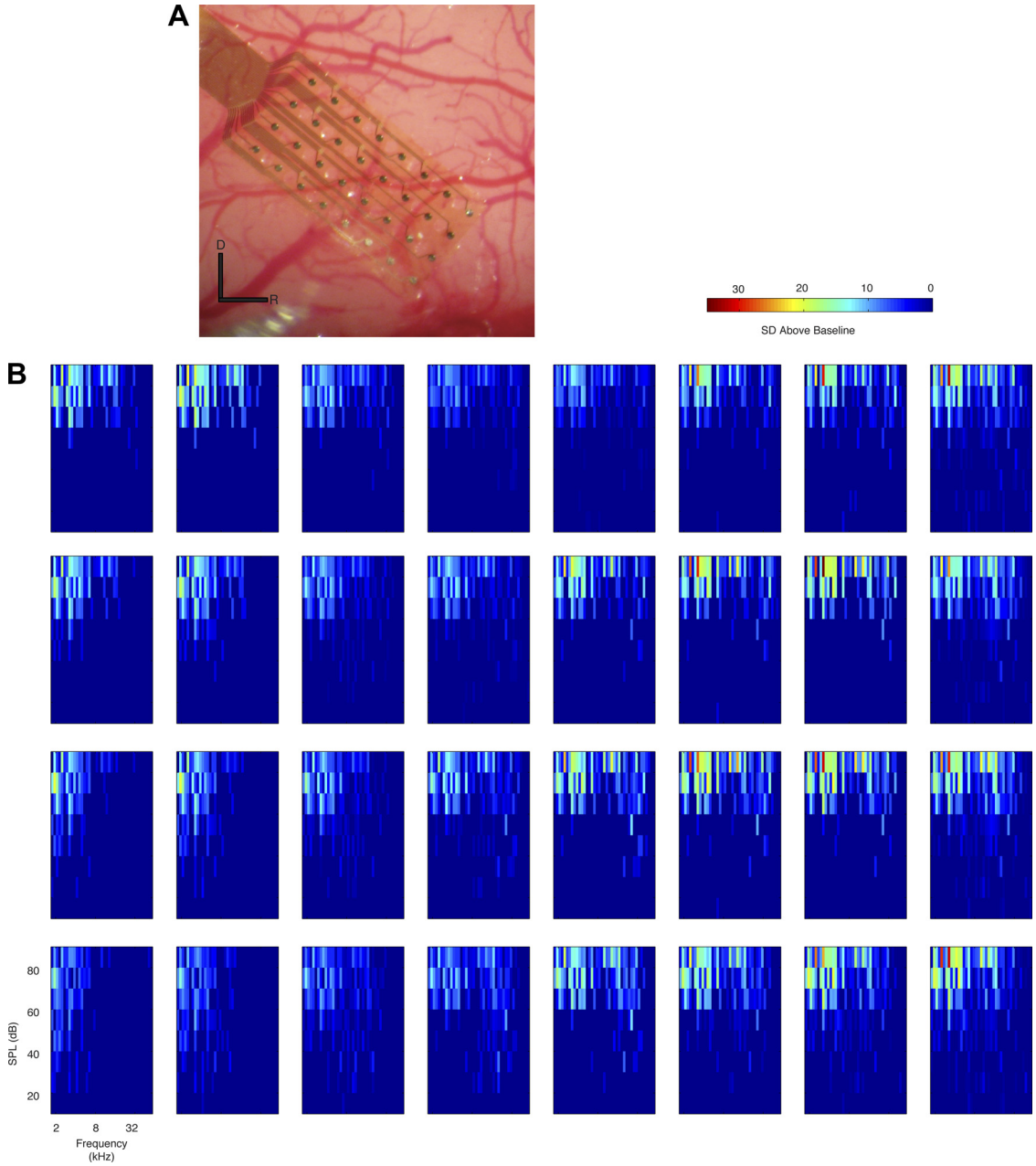

Fig. 6. Topographic distribution of FRAs derived from commercially available passive μECoG recordings. *A*: the lateral surface of a rat's brain, including surface vasculature and the passive NeuroNexus array positioned on the surface of the rat's brain. Scale bars indicate 500 μm, D and R (rostral) indicate the anatomic axes. The FRAs generated from this array are shown in *B*. Red regions indicate frequency-sound level combinations that elicited neural activity that was above baseline; see color bar. Blue regions indicate frequency-sound level combinations that elicited neural activity that was at baseline. Each FRA is normalized relative to the voltage values recorded at that electrode site. The FRAs are organized relative to the spatial position of each recording site on the array. The data shown in this figure are the results from a single animal.

poral-modulation upper-cutoff frequencies were negatively correlated [$r = -0.36 \pm 0.07$ (mean ± SE), $P < 0.01$]. Although temporal-filtering theories would predict a positive correlation between delay and integration time (Oppenheim et al. 1983), this relationship could not be identified in our data set [Fig. 13*F*; $r = -0.06 \pm 0.06$ (mean ± SE), $P > 0.05$].

Functional Correlation

Another advantage afforded by large-scale temporally precise array recordings is the ability to examine the correlations in responses across distant cortical areas to determine functional alignment and segregation of cortical networks. In our final set of analyses, we calculated the pairwise correlation (both signal and noise correlation) between recording sites. Correlograms were calculated as a function of the spatial separation between recordings sites and as a function of the difference between the BF values of recording sites. Figure 14*A* shows the median correlogram as a function of three different spatial separations. Independent of their spatial separation, the correlogram is characteristic of that seen in previous studies (Eggermont 2000; Eggermont et al. 2011): a peak at a time lag of 0 ms with small peaks at longer time lags

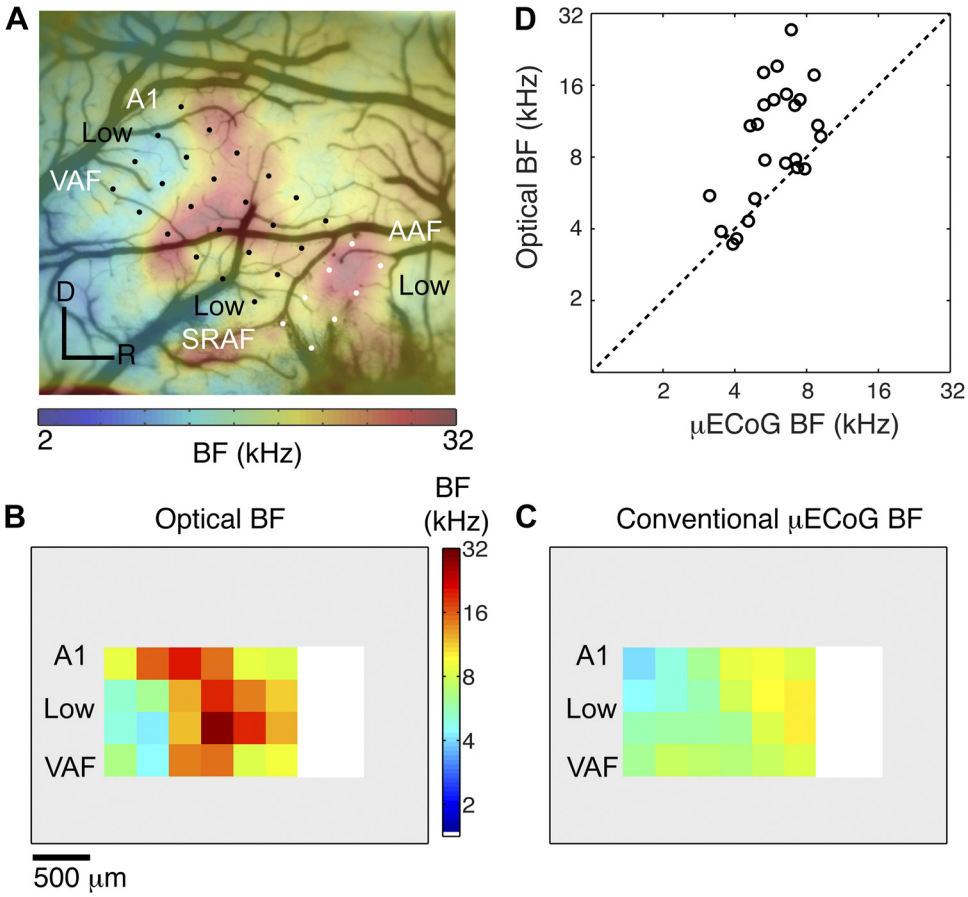

Fig. 7. Correlation between FRAs obtained from IOI and conventional passive μECoG recording. *A*: composite image of the lateral surface of a rat's brain, including surface vasculature and IOI response to tone sequences; the color bar indicates the tone BF. The gray and white dots indicate the locations of each electrode of the array: black dots indicate those electrodes that overlapped with the primary auditory cortex and the area dorsal to A1 (all labeled A1) and VAF, as defined by the IOI. *B* and *C*: the BF maps generated from IOI and μECoG FRA data, respectively. The optical BF was averaged over a spatial region corresponding to the spacing (i.e., 300 × 300 μm) between each recording site of the passive μECoG array. The color bar in *B* indicates the BF (kHz). *D*: a significant (RESULTS) site-by-site correlation between the BF values generated from the conventional passive μECoG FRA and the IOI. The diagonal line is the line of unity for comparison. The white areas in *B* and *C* either were recording sites that were not in the area of interest, or were sites that did not have statistically reliable BFs. The data shown in this figure are the results from a single animal.

corresponding to spindling or the theta range of frequencies (Miller and Schreiner 2000). Nevertheless, as the spatial separation increased, the peak value of the median correlogram decreased. For example, for the data shown in Fig. 14*A*, the peak-correlation value for nearby sites (i.e., 0–1 mm) was 0.2, whereas the peak-correlation value was ~0.02 for sites that were separated by 1–2 mm. Interestingly, at the largest separations (>2 mm), the correlation became negative: peak-correlation values at 0 ms were approximately −0.05. For each of three animals that we tested, the peak-correlation value decreased significantly [2-factor ANOVA (spatial separation × BF); main effect of spatial separation: *rat 1*, $F(2,2297) = 372$; *rat 2*, $F(2,4944) = 909$; $F(2,5044) = 2154$; all $P < 0.05$] with increasing spatial separation.

Because the auditory cortex is tonotopically organized, a reasonable prediction would be that correlation between sites should decrease as a function of their spatial separation and the difference between the BFs of their STRFs. However, because these two parameters do not covary perfectly, we directly tested the relationship between the peak-correlation value and BF difference (Fig. 14*B*). For sites whose BF differences were <3.0 octaves, we found the predicted relationship between BF and correlation. That is, for sites that had similar BFs (i.e., <0.5 octaves), the peak correlation was relatively large (~0.15). But, as the BF difference between sites increased, the correlation decreased and eventually became negative: for sites with BF differences between 0.5 and 1.5 octaves, the correlation was ~0.02, whereas for sites with BF differences between 1.5 and 3 octaves, the correlation was approximately −0.02. This pattern did not hold at the most disparate sites (>3 octaves): the correlation flipped polarity and became positive (~0.02). For each of three animals that we tested, the peak-correlation value was significantly dependent [2-factor ANOVA (spatial separation × BF); main effect of BF: *rat 1*, $F(1,2997) = 46$; *rat 2*, $F(1,4944) = 196$; $F(1,5044) = 396$; all $P < 0.05$] on BF.

The functional relationship between spatial separation, BF difference, and the peak-correlation value can be seen in Fig. 14*C*. Similar to previous findings (Bao et al. 2003), at nearby sites, correlation values were highest for sites with the most similar BFs. As the BF difference increased, the peak-correlation value maintained a similar pattern, although the peak-correlation value decreased. At intermediate separations (i.e., 1–2 mm), the peak-correlation value was small and independent of BF difference. At the largest separations (i.e., >2 mm), the relationship between BF difference and peak-correlation value was complex. Nevertheless, these peak-correlation values tended to be larger than those seen at intermediate separations (i.e., 1–2 mm). Once again, for each of three animals that we tested, the peak-correlation value was significantly modulated [2-factor ANOVA (spatial separation × BF); interaction between spatial separation and BF: *rat 1*, $F(2,1) = 41$; *rat 2*, $F(2,1) = 40$; $F(2,1) = 24$; all $P < 0.05$] by both spatial separation and BF difference.

Finally, because the electrodes along the columns and rows differentially transmitted information (i.e., the column electrodes had signals that were multiplexed together, whereas those along the rows transmitted signals on independent wires),

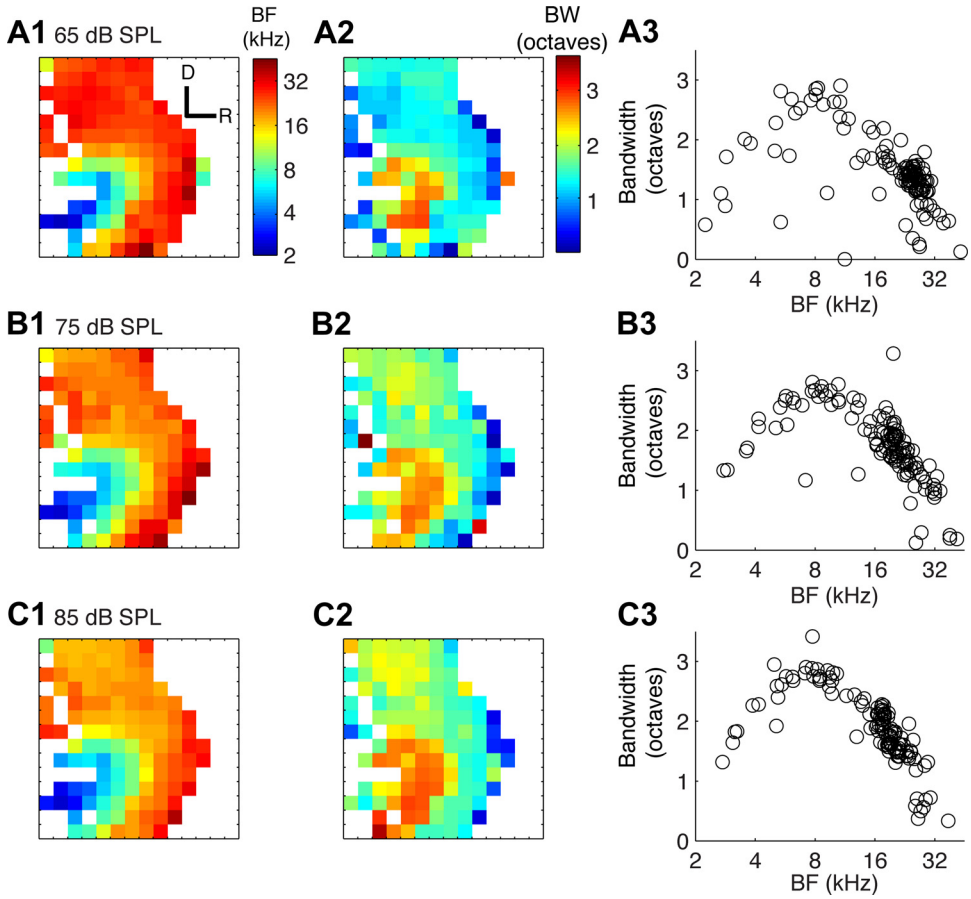

Fig. 8. Topographic organization and relationship between BF and bandwidth (BW) measured with the custom μECoG array. *A1* and *A2*: position maps for tone BF and BW, respectively, derived from the FRA obtained at a sound level of 65 dB SPL. Scale bars indicate 500 μm, D and V anatomic axes. Color bars indicate range of values in all corresponding maps. *A3*: an inverted "U-shaped" relationship is observed between BF vs. BW measured at each cortical site. *B1–B3* and *C1–C3* follow the same convention as in *A1–A3*; however, data are obtained at sound levels of 75 and 85 dB SPL, respectively. The data shown in this figure are the results from a single animal, same animal as in Fig. 4.

our correlation values might have depended on the transmission route. To address this issue, we independently calculated correlation data along a column of an array and independently along a row of an array. We found that the distribution of correlation values overlapped ($P > 0.05$; data not shown), which indicated that, on average, the method of transmission did not bias the neural correlations between the electrodes.

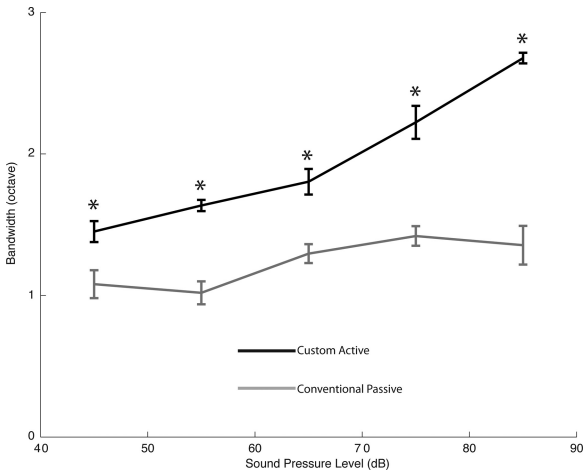

Fig. 9. A comparison of the FRA BW selectivity between custom active and conventional passive μECoG arrays. The median BW for each array is plotted as a function of sound level. Error bars indicate the standard error obtained via bootstrapping across measurements (MATERIALS AND METHODS). *Sound levels in which the BWs of custom vs. conventional array responses were significantly different ($P < 0.001$; rank-sum test).

DISCUSSION

Our understanding of the large-scale population dynamics of neural activity is not complete. This gap in our knowledge is due, in part, to our inability to record simultaneously from large regions of the auditory cortex with high spatial and temporal resolution and large cortical area coverage. Although providing important principles, previous single-unit and electrocortigraphical studies have been limited to simultaneous recordings from fewer cortical sites (Eggermont et al. 2011; Mesgarani and Chang 2012; Ogawa et al. 2011; Owens et al. 1995; Pasley et al. 2012; Takahashi et al. 2003). Large-scale recordings have been obtained with intrinsic imaging; however, these recordings reflect slow metabolic activity and not temporally precise neural activity (Besle et al. 2011; Ebner and Chen 1995). Finally, studies using voltage-sensitive dyes (Horikawa et al. 2001; Kubota et al. 2012; Sawatari et al. 2011) are limited because, whereas this technique allows for recordings from large areas of the brain, current dyes have relatively poor temporal resolution and signal-to-noise ratio. Here, we demonstrated a new approach that is not invasive to cortical tissue and allows for large-scale mapping of sound-response properties with high spatial and temporal precision.

We found that the tone-frequency response organization revealed by our custom active μECoG array was very similar to that revealed by IOI and substantially better than a conventional passive μECoG array. This result validates our active μECoG array as a reliable probe for assessing functional properties and organization of the auditory cortex. Moreover, we also found that our custom array was an appropriate probe

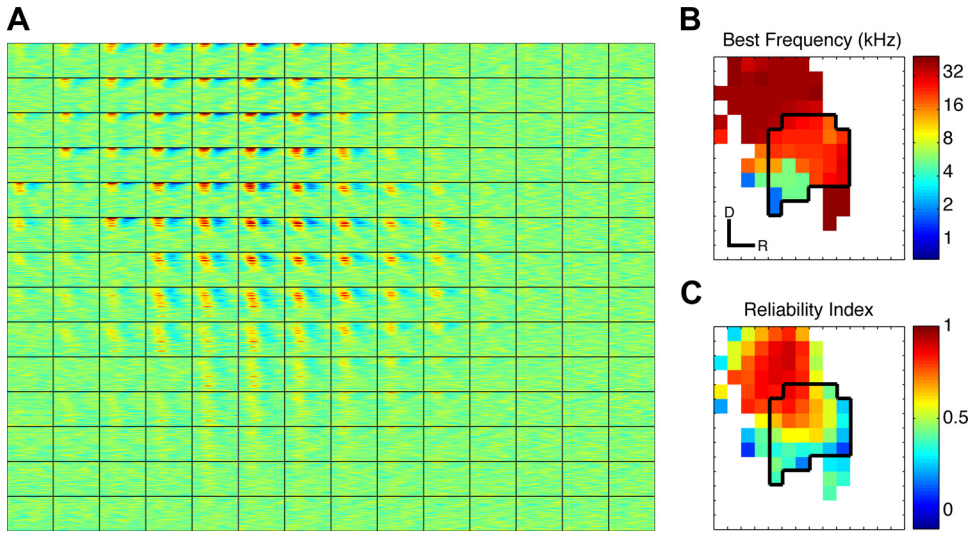

Fig. 10. Topographic distribution of STRFs and BFs derived from custom active-μECoG-array responses. *A*: the topographic organization of STRFs that were generated from each recording site on the array. Each square demarcates the relative location of each electrode and the STRF that was generated from the neural activity recorded at that site. For each STRF, delay in milliseconds is plotted on the *x*-axis, and frequency in octaves is plotted on the *y*-axis. Blue regions indicate excitatory voltage responses were temporally phase-locked with the auditory stimulus, whereas blue values indicate suppressive/inhibitory responses (see Fig. 11 for typical STRF patterns). The color scale on all STRFs is normalized relative to the recording site with the strongest response. The reliability of each STRF is shown in *B* for each recording site. The value of each STRFs reliability is indicated by the color bar: STRFs with lowest reliability are blue, and those with highest reliabilities are dark red. *C*: the topographic organization of BF. The BF from each recording site was calculated from the STRFs shown in *A*. The BF of each site is indicated by the color bar: sites with ~1-kHz BFs are dark blue, and those with ~32-kHz BFs are dark red. The data shown in this figure are the results from a single animal. The pure-tone BF responses and various STRF response parameters for this animal are shown in Figs. 5 and 12, respectively.

to test the temporal precision of neural responses to more ethologically relevant dynamically modulated sounds.

In this study, we identified novel cortical-field differences using the active μECoG array. First, the pure-tone BF responses obtained with IOI and active-μECoG methodologies were correlated and had similar tonotopic organization over a large cortical area, including A1, an area dorsal to A1 and VAF. Second, most sites in VAF lacked significant STRFs (e.g., Figs. 10 and 12), although the same sites exhibited clearly defined responses to tones for both the IOI and μECoG recordings (Figs. 2 and 5). Together, these findings indicate that A1 represents sound frequency with a high degree of

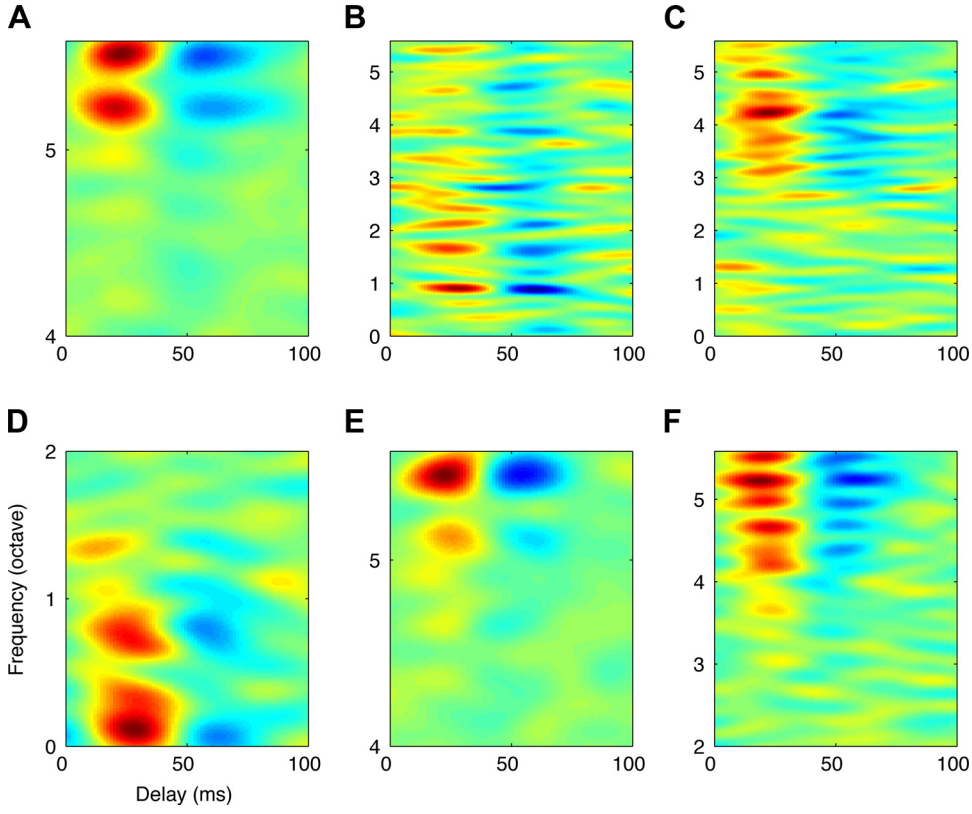

Fig. 11. Examples of STRFs from the primary auditory cortex. *A–F*: each panel shows a STRF generated from a different recording site. As indicated by the color bar, increasingly red regions indicate spectrotemporal combinations in which the μECoG signal was increasing, whereas increasingly blue regions indicate spectrotemporal combinations in which the μECoG signal was at decreasing. For both, increases and decreases were temporally phase-locked with the auditory stimulus. The STRFs have been normalized relative to the maximum values.

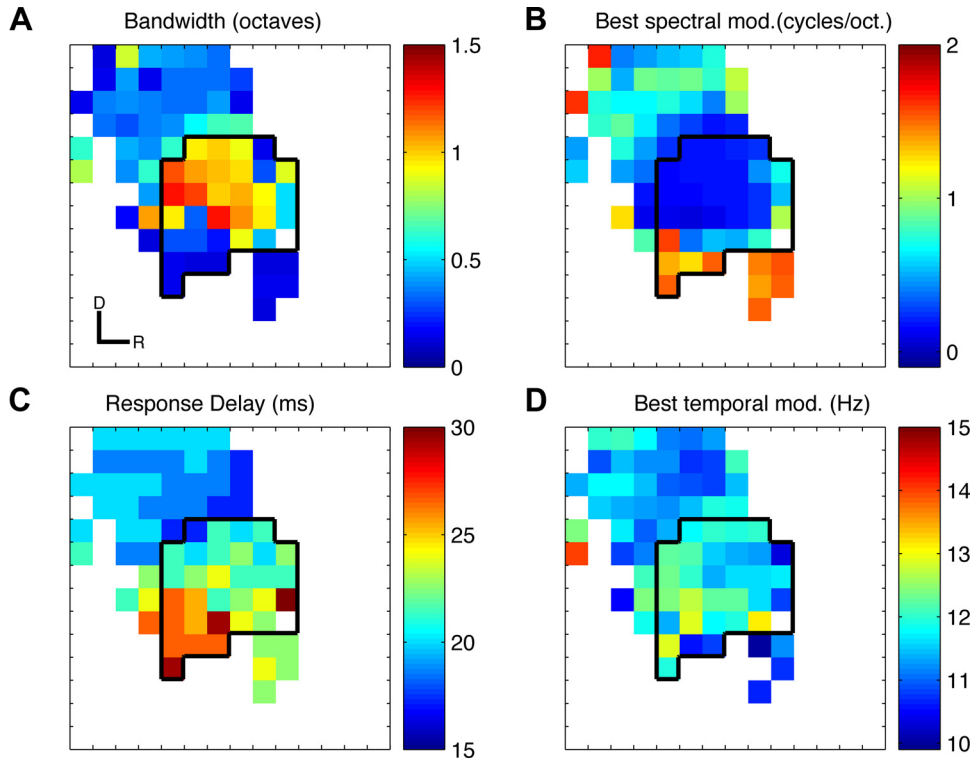

Fig. 12. Topographic organization of STRF parameters. *A*: the organization of STRF BW in units of octaves. *B*: the organization of the best spectral modulation in units of Hertz/octave. *C*: the organization of response delay in units of milliseconds. *D*: the organization of the best temporal modulation in Hertz. The color bar next to each panel indicates the respective range of values. See MATERIALS AND METHODS for details on how these parameters were calculated. In each panel, the thick black line delineates the borders of the primary auditory cortex and the VAF. The spatial orientation of the data in *B–D* is the same as that shown in *A*. The data shown in this figure are the results from a single animal. The boundaries between the primary auditory cortex and the VAF were determined by the direction of the BF gradients in the optical image, as described previously (Higgins et al. 2010).

temporal precision and phase-locking to envelope modulations, whereas VAF represents sound frequency with a low degree of temporal precision. This is consistent with reports of low vector strength for multiunit VAF spike-rate responses to periodically modulated sound sequences compared with A1 in the rat (Engineer et al. 2014). These observations build on and are consistent with prior studies reporting slower response peak latencies for VAF compared with A1 (Funamizu et al. 2013; Polley et al. 2007).

One possible explanation for these cortical-field differences is that tone-based responses do not require the same level of temporal precision and phase-locking as required for the STRFs. STRFs reflect phase-locked neural activity to sound modulations that requires substantially higher temporal re-

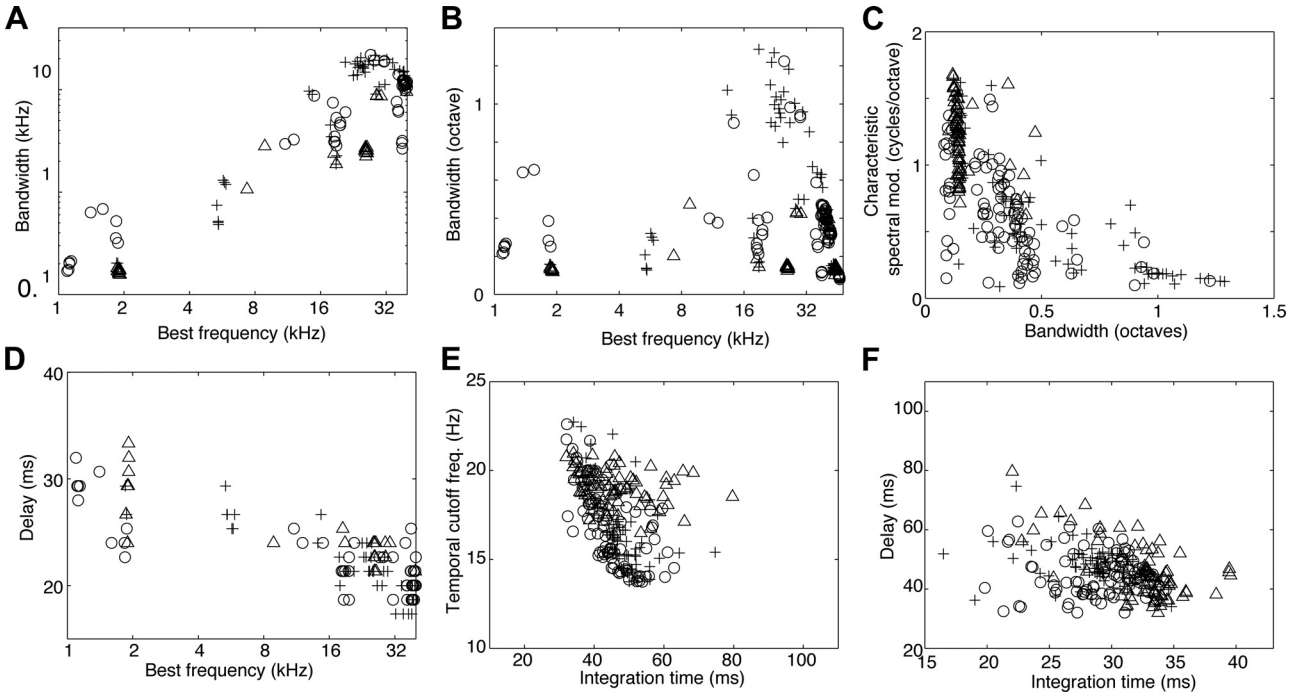

Fig. 13. Correlation between STRF parameters. The correlations between different *A–F*: STRF parameters are shown in each of the panels. Each symbol in each graph represents the data value (e.g., BF and BW for *A*) generated from the STRF at a single recording site. The different symbols (circle, triangle, and cross) represent data from different animals.

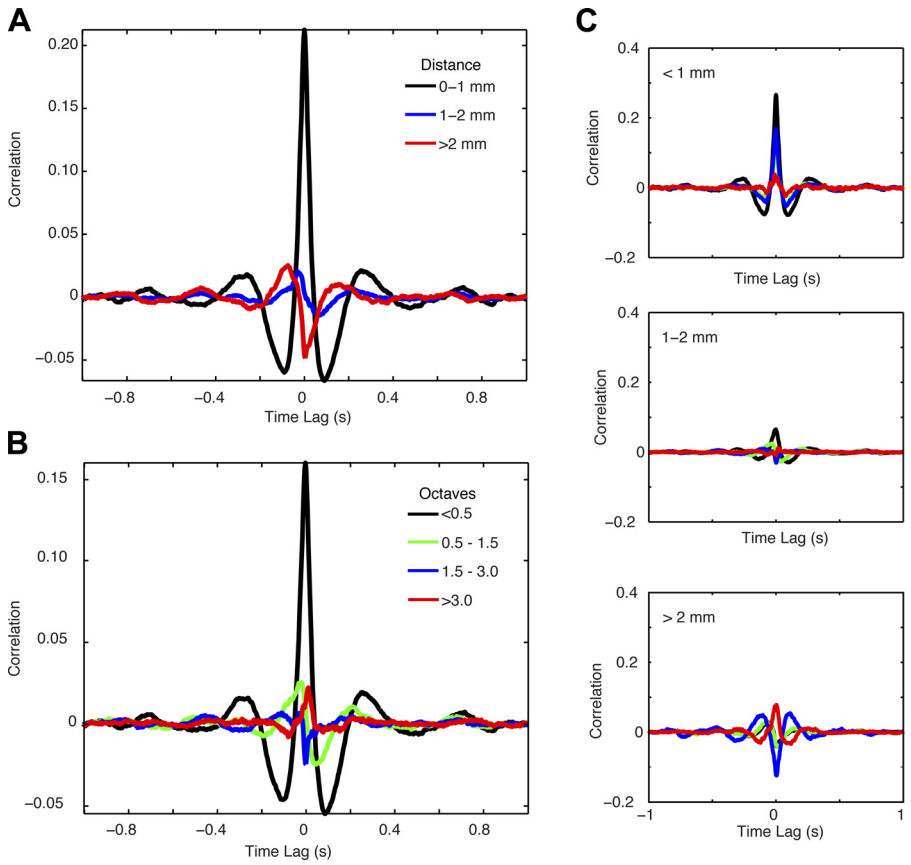

Figure 14, Escabi, 2014

Fig. 14. The pairwise correlation between recording sites was dependent on their spatial separation and the difference between the STRF BFs for each site. *A*: the median cross-correlation functions as a function of the spatial separation between recording sites. *B*: the median cross-correlation functions as a function of the BF difference. *C*: the interdependence between spatial separation and BF difference. In each plot, the spatial separation is held constant, whereas the cross-correlation functions are plotted as a function of BF difference. See *B* for the color code of BF difference. For all of the panels, each cross-correlation function represents the median function that was calculated from the subset of recording sites that had significant STRFs for each combination of spatial separation and BF difference. The data shown in this figure are the results from a single animal.

sponse precision to produce significant response fields. As seen from Fig. 10, STRF (phase-locking) reliability varied across the dorsal-to-ventral axis, such that sites in A1 were the most reliable, whereas sites in VAF had low reliability and insignificant STRFs. Such a difference could in theory be due to lower response amplitudes for tone vs. DMR STRFs (Pienkowski and Eggermont 2011). Because reliable tone FRAs were elicited in VAF, the lack of STRFs in this region cannot be trivially attributed to a lack of responsiveness. Instead, the differences may be due to poorer response-timing precision and/or reliability of these ventral sites. Indeed, STRF reliability was highest in the region dorsal to A1 but lowest on average in VAF. This dorsal-ventral difference may have important functional consequences: A1 and the dorsal area may employ a robust timing code, whereas VAF may transmit information through slower changes in firing rate.

The recording array and reconstructed STRFs resolved distinct neurophysiological responses across neighboring recording sites, as evident from differences in receptive fields in nearby recording sites. μECoG STRFs and intrinsic metabolic responses measured at the same cortical sites had similar BFs and topographic organization (Fig. 5). Prior current source density analyses find the largest local field potential responses to dynamic sounds reside within the thalamic input layers of auditory cortex (Szymanski et al. 2011). Although we cannot determine the primary source of the μECoG STRF responses in the present study, the spatial resolution and organization of μECoG responses in the auditory cortex is consistent with that observed with local field potential responses to pure tones and dynamic sounds (Eggermont et al. 2011; Ohl et al. 2000). Several spectral and temporal features of the μECoG STRF changed systematically with BF (Figs. 12 and 13), as predicted from previous single and multiunit studies (Atencio and Schreiner 2012; Cheung et al. 2001; Eggermont et al. 2011) and subcortical stations of the auditory pathway (Rodriguez et al. 2010a, 2010b). Our study builds on these prior studies because we demonstrated that reliable, phase-locked responses to sound features can be generated from μECoG-level signals.

Sensory-driven response-feature correlations are more likely to occur between neurons and regions with similar response properties (Atencio and Schreiner 2010; deCharms and Merzenich 1996; Tomita and Eggermont 2005) that are also connected by short- and long-range corticocortical connections (Chisum and Fitzpatrick 2004; Read et al. 2001). Accordingly, in the auditory cortex, neighboring neurons and neurons located more than 1 mm away that have similar BFs (within ± ⅓ octave) are anatomically connected (Read et al. 2001). Our approach allowed us to test the response correlation between electrode sites across a large range of cortical positions covered by the recording array. As indicated with other methodologies, by far the strongest correlations occurred between neighboring cortical positions with similar BFs (Fig. 14). However, consistent with previous studies (Brosch and Schreiner 1999; Eggermont 2000), we also found that relatively high correlations occurred between positions separated by large distances, and these were not restricted to sites with similar BFs. These correlations were likely driven by higher-order receptive-field properties other than BF (Brosch and Schreiner 1999) and may underlie the ensemble or population coding needed to create unified perceptual representations of auditory stimuli

(deCharms and Merzenich 1996; Eggermont 1997; 2000; Griffiths and Warren 2004; King and Nelken 2009).

Compared with IOI, our active μECoG arrays have comparable spatial resolution over a large recording area (Fig. 5). However, unlike IOI, which reflects slow metabolic activity (Besle et al. 2011; Ebner and Chen 1995), the arrays measure neural signals on short time scales and can be used to assess precise timing of stimulus-response functions (i.e., STRFs; Figs. 10–13) or precisely correlated network activity (Fig. 14). As demonstrated, our custom active μECoG array offers better spatial selectivity (compare Figs. 5 and 7) and thus produces more accurate sensory maps over a larger recording area than currently available passive μECoG technologies. Furthermore, unlike IOI, which requires tens of minutes of neural data acquisition to measure BF organization at a single sound level, cortical BF organization can be derived rapidly with a single response trial of the active μECoG array (Figs. 3 and 4; 13.5-s acquisition time for one sound level), allowing measurements of cortical organization at multiple sound levels in as little as 1.5 min.

Overall, this study indicated the promising future for using μECoG micro-fabricated flexible arrays to reveal new principles of auditory organization in the cortex. Whereas there are some potential disadvantages of this approach, including potentially higher cost and increased computational burden for analysis, these obstacles can be overcome. Reliable flexible encapsulation of implanted active circuitry remains a challenging area for future research that we are actively pursuing.

The current flexible electrode array was a product of recent advances in materials science and micro-fabrication that allow active circuitry to be built directly into a flexible substrate. This intimate integration allowed for a high-resolution interface with the cortical surface and ultimately will enable low-noise amplification of signals from thousands of discrete electrodes to be recorded without requiring thousands of wires. The spacing of this array, currently 1 electrode per 250 μm, can be reduced using more advanced semiconductor fabrication techniques and is essentially only limited by the available resolution of the neural signals. In the future, it will be important to develop novel coatings and materials to extend the device encapsulation lifetime to allow for long-term chronic recordings. The current version of this array minimizes the interface wires (i.e., 29) to record high-fidelity signals from 196 electrodes and, therefore, is the first necessary step to adapt these arrays for future chronic implantation and continuous recording in freely behaving animals in future studies.

ACKNOWLEDGMENTS

We thank Heather Hersh for helpful comments on the preparation of this manuscript.

GRANTS

This research was supported by grants from the National Institute on Deafness and Other Communications Disorders and Boucai Hearing Restoration Fund to Y. E. Cohen. This material is based upon work supported by the National Science Foundation under grant DMI-0328162 and the US Department of Energy, Division of Materials Sciences under Award No. DE-FG02-07ER46471, through the Materials Research Laboratory and Center for Microanalysis of Materials (DE-FG02-07ER46453) at the University of Illinois at Urbana-Champaign. J. A. Rogers acknowledges a National Security Science and Engineering Faculty Fellowship. B. Litt is supported by National Institute of Neurological Disorders and Stroke Grants (RO1-NS-041811, R01-NS-48598), the Dr. Michel and Mrs. Anna Mirowski Discovery Fund for Epilepsy Research, and the Julie's Hope Award from Citizens United for Research in Epilepsy (CURE). J. Viventi is supported by a Taking Flight Award from CURE and NYU Wireless.

DISCLOSURES

No conflicts of interest, financial or otherwise, are declared by the author(s).

AUTHOR CONTRIBUTIONS

Author contributions: M.A.E., H.L.R., J.V., D.-H.K., N.C.H., D.S., Y.-S.K., A.E.A., J.V.d.S., Y.H., M.L., J.W., J.A.R., B.L., and Y.E.C. conception and design of research; M.A.E., H.L.R., J.V., N.C.H., D.S., A.S.L., and Y.E.C. performed experiments; M.A.E., H.L.R., N.C.H., D.S., A.M.G., J.F.B., and M.C. analyzed data; M.A.E., H.L.R., N.C.H., D.S., and Y.E.C. interpreted results of experiments; M.A.E., H.L.R., J.V., N.C.H., D.S., and Y.E.C. prepared figures; M.A.E., H.L.R., J.V., and Y.E.C. drafted manuscript; M.A.E., H.L.R., J.V., D.-H.K., N.C.H., D.S., A.S.L., A.M.G., J.F.B., M.C., Y.-S.K., A.E.A., J.V.d.S., Y.H., M.L., J.W., J.A.R., B.L., and Y.E.C. edited and revised manuscript; M.A.E., H.L.R., J.V., D.-H.K., N.C.H., D.S., A.S.L., A.M.G., J.F.B., M.C., Y.-S.K., A.E.A., J.V.d.S., Y.H., M.L., J.W., J.A.R., B.L., and Y.E.C. approved final version of manuscript.

REFERENCES

Atencio CA, Schreiner CE. Columnar connectivity and laminar processing in cat primary auditory cortex. *PLos One* 3: e9521, 2010.

Atencio CA, Schreiner CE. Spectrotemporal processing in spectral tuning modules of cat primary auditory cortex. *PLos One* 7: e3153, 2012.

Bao S, Chang EF, Davis JD, Gobeske KT, Merzenich MM. Progressive degradation and subsequent refinement of acoustic representation in the adult auditory cortex. *J Neurosci* 23: 10765–10775, 2003.

Besle J, Schevon CA, Mehta AD, Lakatos P, Goodman RR, McKhann GM, Emerson RG, Schroeder CE. Tuning of the human neocortex to the temporal dynamics of attended events. *J Neurosci* 31: 3176–3185, 2011.

Brosch M, Schreiner CE. Correlations between neural discharges are related to receptive field properties in cat primary auditory cortex. *Eur J Neurosci* 11: 3517–3530, 1999.

Centanni TM, Booker AB, Sloan AM, Chen F, Maher BJ, Carraway RS, Khodaparast N, Rennaker R, Loturco JJ, Kilgard MP. Knockdown of the dyslexia-associated gene Kiaa0319 impairs temporal responses to speech stimuli in rat primary auditory cortex. *Cereb Cortex* 24: 1753–1766, 2014.

Cheung SW, Bedenbaugh PH, Nagarajan SS, Schreiner CE. Functional organization of squirrel monkey primary auditory cortex: reponses to pure tones. *J Neurophysiol* 85: 1732–1749, 2001.

Chisum HJ, Fitzpatrick D. The contribution of vertical and horizontal connections to the receptive field center and surround in V1. *Neural Netw* 17: 681–693, 2004.

deCharms RC, Blake DT, Merzenich MM. Optimizing sound features for cortical neurons. *Science* 280: 1439–1444, 1998.

deCharms RC, Merzenich MM. Primary cortical representation of sounds by the coordination of action-potential timing. *Nature* 381: 610–613, 1996.

DePireux DA, Simon JZ, Klein DJ, Shamma SA. Spectro-temporal response field characterization with dynamic ripples in ferret primary auditory cortex. *J Neurophysiol* 85: 1220–1234, 2001.

Dorf RC, Bishop RM. *Modern Control Systems*. Reading, MA: Addison-Wesley, 1995.

Doron NN, Ledoux JE, Semple MN. Redefining the tonotopic core of rat auditory cortex: physiological evidence for a posterior field. *J Comp Neurol* 453: 345–360, 2002.

Ebner TJ, Chen G. Use of voltage-sensitive dyes and optical recordings in the central nervous system. *Prog Neurobiol* 46: 463–506, 1995.

Eggermont JJ. Firing rate and firing synchrony distinguish dynamic from steady state sound. *Neuroreport* 8: 2709–2713, 1997.

Eggermont JJ. Sound-induced synchronizaion of neural activity between and within three auditory cortical areas. *J Neurophysiol* 83: 2708–2722, 2000.

Eggermont JJ, Aertsen AM, Hermes DJ, Johannesma PI. Spectro-temporal characterization of auditory neurons: redundant or necessary? *Hear Res* 5: 109–121, 1981.

Eggermont JJ, Munguia R, Pienkowski M, Shaw G. Comparison of LFP-based and spike-based spectro-temporal receptive fields and cross-correlation in cat primary auditory cortex. *PLos One* 6: e20046, 2011.

Engineer CT, Centanni TM, Im KW, Borland MS, Moreno NA, Carraway RS, Wilson LG, Kilgard MP. Degraded auditory processing in a rat model of autism limits the speech representation in non-primary auditory cortex. *Dev Neurobiol*. In press, 2014.

Escabi MA, Higgins NC, Galaburda AM, Rosen GD, Read HL. Early cortical damage in rat somatosensory cortex alters acoustic feature representation in primary auditory cortex. *Neuroscience* 150: 970–983, 2007.

Escabi MA, Read HL. Neural mechanisms for spectral analysis in the auditory midbrain, thalamus, and cortex. *Int Rev Neurobiol* 70: 207–252, 2005.

Escabí MA, Read HL. Representation of spectrotemporal sound information in the ascending auditory pathway. *Biol Cybern* 89: 350–362, 2003.

Escabí MA, Schreiner CE. Nonlinear spectrotemporal sound analysis by neurons in the auditory midbrain. *J Neurosci* 22: 4114–4131, 2002.

Fritz J, Shamma S, Elhilali M, Klein D. Rapid task-related plasticity of spectrotemporal receptive fields in primary auditory cortex. *Nat Neurosci* 6: 1216–1223, 2003.

Funamizu A, Kanzaki R, Takahashi H. Pre-attentive, context-specific representation of fear memory in the auditory cortex of rat. *PLos One* 8: e63655, 2013.

Geffen MN, Gervain J, Werker JF, Magnasco MO. Auditory perception of self-similarity in water sounds. *Front Integr Neurosci* 5: 15, 2011.

Griffiths TD, Warren JD. What is an auditory object? *Nat Rev Neurosci* 5: 887–892, 2004.

Higgins NC, Escabi MA, Rosen GD, Galaburda AM, Read HL. Spectral processing deficits in belt auditory cortex following early postnatal lesions of somatosensory cortex. *Neuroscience* 153: 535–549, 2008.

Higgins NC, Storace DA, Escabi MA, Read HL. Specialization of binaural responses in ventral auditory cortices. *J Neurosci* 30: 14522–14532, 2010.

Horikawa J, Hess A, Nasu M, Hosokawa Y, Scheich H, Taniguchi I. Optical imaging of neural activity in multiple auditory cortical fields of guinea pigs. *Neuroreport* 12: 3335–3339, 2001.

Kalatsky VA, Polley DB, Merzenich MM, Schreiner CE, Stryker MP. Fine functional organization of auditory cortex revealed by Fourier optical imaging. *Proc Natl Acad Sci U S A* 102: 13325–13330, 2005.

Kalatsky VA, Stryker MP. New paradigm for optical imaging: temporally encoded maps of intrinsic signal. *Neuron* 38: 529–545, 2003.

King AJ, Nelken I. Unraveling the principles of auditory cortical processing: can we learn from the visual system? *Nat Neurosci* 12: 698–701, 2009.

Kubota M, Miyamoto A, Hosokawa Y, Sugimoto S, Horikawa J. Spatiotemporal dynamics of neural activity related to auditory induction in the core and belt fields of guinea-pig auditory cortex. *Neuroreport* 23: 474–478, 2012.

Linden JF, Liu RC, Sahani M, Schreiner CE, Merzenich MM. Spectrotemporal structure of receptive fields in areas AI and AAF of mouse auditory cortex. *J Neurophysiol* 90: 2660–2675, 2003.

Machens CK, Wehr MS, Zador AM. Linearity of cortical receptive fields measured with natural sounds. *J Neurosci* 24: 1089–1100, 2004.

Mesgarani N, Chang EF. Selective cortical representation of attended speaker in multi-talker speech perception. *Nature* 485: 233–236, 2012.

Miller LM, Escabí MA, Read HL, Schreiner CE. Feature selectivity and interneuronal cooperation in the thalamocortical system. *J Neurosci* 21: 8136–8144, 2001.

Miller LM, Escabí MA, Read HL, Schreiner CE. Spectrotemporal receptive fields in the lemniscal auditory thalamus and cortex. *J Neurophysiol* 87: 516–527, 2002.

Miller LM, Schreiner CE. Stimulus-based state control in the thalamocortical system. *J Neurosci* 20: 7011–7016, 2000.

Miyakawa A, Gibboni R, Bao S. Repeated exposure to a tone transiently alters spectral tuning bandwidth of neurons in the central nucleus of inferior colliculus in juvenile rats. *Neuroscience* 230: 114–120, 2013.

Norena A, Gourevitch B, Pienkowski M, Shaw G, Eggermont JJ. Increasing spectrotemporal sound density reveals an octave-based organization in cat primary auditory cortex. *J Neurosci* 28: 8885–8896, 2008.

Ogawa T, Riera J, Goto T, Sumiyoshi A, Nonaka H, Jerbi K, Bertrand O, Kawashima R. Large-scale heterogeneous representation of sound attributes in rat primary auditory cortex: from unit activity to population dynamics. *J Neurosci* 31: 14639–14653, 2011.

Ohl FW, Scheich H, Freeman WJ. Topographic analysis of epirdural pure-tone-evoked potentials in gerbil auditory cortex. *J Neurophysiol* 83: 3123–3132, 2000.

Oppenheim AV, Willsky AS, Young IT. *Signals and Systems*. Englewood Cliffs, NJ: Prentice-Hall, 1983.

Owens AL, Denison TJ, Versnel H, Rebbert M, Peckerar M, Shamma SA. Multi-electrode array for measuring evoked potentials from surface of ferret primary auditory cortex. *J Neurosci Methods* 58: 209–220, 1995.

Pasley BN, David SV, Mesgarani N, Flinker A, Shamma S, Crone NE, Knight RT, Chang EF. Reconstructing speech from human auditory cortex. *PLoS Biol* 10: e1001251, 2012.

Pickles JO. *An Introduction to the Physiology of Hearing*. New York: Academic, 1988.

Pienkowski M, Eggermont JJ. Sound frequency representation in primary auditory cortex is level tolerant for moderately loud, complex sounds. *J Neurophysiol* 106: 1016–1027, 2011.

Polley DB, Read HL, Storace DA, Merzenich MM. Multiparametric auditory receptive field organization across five cortical fields in the albino rat. *J Neurophysiol* 97: 3621–3638, 2007.

Qiu A, Schreiner CE, Escabí MA. Gabor analysis of auditory midbrain receptive fields: spectro-temporal and binaural composition. *J Neurophysiol* 90: 456–476, 2003.

Read HL, Winer JA, Schreiner CE. Modular organization of intrinsic connections associated with spectral tuning in cat auditory cortex. *Proc Natl Acad Sci U S A* 98: 8042–8047, 2001.

Reimer A, Hubka P, Engel AK, Kral A. Fast propagating waves within the rodent auditory cortex. *Cereb Cortex* 21: 166–177, 2011.

Rodriguez FA, Chen C, Read HL, Escabí MA. Neural modulation tuning characteristics scale to efficiently encode natural sound statistics. *J Neurosci* 30: 15969–15980, 2010a.

Rodriguez FA, Read HL, Escabi MA. Spectral and temporal modulation tradeoff in the inferior colliculus. *J Neurophysiol* 103: 887–903, 2010b.

Rutkowski RG, Miasnikov AA, Weinberger NM. Characterisation of multiple physiological fields within the anatomical core of rat auditory cortex. *Hear Res* 181: 116–130, 2003.

Sawatari H, Tanaka Y, Takemoto M, Nishimura M, Hasegawa K, Saitoh K, Song WJ. Identification and characterization of an insular auditory field in mice. *Eur J Neurosci* 34: 1944–1952, 2011.

Storace DA, Higgins NC, Chikar JA, Oliver DL, Read HL. Gene expression identifies distinct ascending glutamatergic pathways to frequency-organized auditory cortex in the rat brain. *J Neurosci* 32: 15759–15768, 2012.

Storace DA, Higgins NC, Read HL. Thalamic label patterns suggest primary and ventral auditory fields are distinct core regions. *J Comp Neurol* 518: 1630–1646, 2010.

Storace DA, Higgins NC, Read HL. Thalamocortical pathway specialization for sound frequency resolution. *J Comp Neurol* 519: 177–193, 2011.

Szymanski FD, Rabinowitz NC, Magri C, Panzeri S, Schnupp JW. The laminar and temporal structure of stimulus information in the phase of field potentials of auditory cortex. *J Neurosci* 31: 15787–15801, 2011.

Takahashi H, Ejiri T, Nakao M, Nakamura N, Kaga K, Herve T. Microelectrode array on folding polyimide ribbon for epidural mapping of functional evoked potentials. *IEEE Trans Biomed Eng* 50: 510–516, 2003.

Takahashi H, Yokota R, Funamizu A, Kose H, Kanzaki R. Learning-stage-dependent, field-specific, map plasticity in the rat auditory cortex during appetitive operant conditioning. *Neuroscience* 199: 243–258, 2011.

Tomita M, Eggermont JJ. Cross-correlation and joint spectro-temporal receptive field properties in auditory cortex. *J Neurophysiol* 93: 378–392, 2005.

Viventi J, Kim DH, Moss JD, Kim YS, Blanco JA, Annetta N, Hicks A, Xiao J, Huang Y, Callans DJ, Rogers JA, Litt B. A conformal, bio-interfaced class of silicon electronics for mapping cardiac electrophysiology. *Sci Transl Med* 2: 24ra22, 2010.

Viventi J, Kim DH, Vigeland L, Frechette ES, Blanco JA, Kim YS, Avrin AE, Tiruvadi VR, Hwang SW, Vanleer AC, Wulsin DF, Davis K, Gelber CE, Palmer L, Van der Spiegel J, Wu J, Xiao J, Huang Y, Contreras D, Rogers JA, Litt B. Flexible, foldable, actively multiplexed, high-density electrode array for mapping brain activity in vivo. *Nat Neurosci* 14: 1599–1605, 2011.

von der Behrens W, Bauerle P, Kossl M, and Gaese BH. Correlating stimulus-specific adaptation of cortical neurons and local field potentials in the awake rat. *J Neurosci* 29: 13837–13849, 2009.